

# Complete Pronghorn Electrochemistry Modeling Improvements for Corrosion and Plating Modeling

INL/RPT-25-88131

NEAMS

M3 Milestone Report

---

SEPTEMBER 2025

---

**Mauricio Tano, Samuel Walker, and Ramiro Freile**

*Thermal Fluids Systems Methods and Analysis*

**Chaitanya Bhave and Parikshit Bajpai**

*Computational Mechanics and Materials*



#### DISCLAIMER

This information was prepared as an account of work sponsored by an agency of the U.S. Government. Neither the U.S. Government nor any agency thereof, nor any of their employees, makes any warranty, expressed or implied, or assumes any legal liability or responsibility for the accuracy, completeness, or usefulness, of any information, apparatus, product, or process disclosed, or represents that its use would not infringe privately owned rights. References herein to any specific commercial product, process, or service by trade name, trade mark, manufacturer, or otherwise, does not necessarily constitute or imply its endorsement, recommendation, or favoring by the U.S. Government or any agency thereof. The views and opinions of authors expressed herein do not necessarily state or reflect those of the U.S. Government or any agency thereof.

# **Complete Pronghorn Electrochemistry Modeling Improvements for Corrosion and Plating Modeling**

## **M3 Milestone Report**

**Mauricio Tano, Samuel Walker, and Ramiro Freile**  
**Thermal Fluids Systems Methods and Analysis**  
**Chaitanya Bhave and Parikshit Bajpai**  
**Computational Mechanics and Materials**

**September 2025**

**Idaho National Laboratory**  
**Advanced Scientific Computing**  
**Idaho Falls, Idaho 83415**

**<http://www.inl.gov>**

**Prepared for the**  
**U.S. Department of Energy**  
**Office of Nuclear Energy**  
**Under DOE Idaho Operations Office**  
**Contract DE-AC07-05ID14517**

*Page intentionally left blank*

## **ABSTRACT**

This report presents a comprehensive investigation into the corrosion mechanisms and noble metal plating behaviors in molten salt reactors (MSRs) through multiphysics modeling using the MOOSE framework. We improve the integrated Poisson-Nernst-Planck (PNP) model developed in FY24 to capture the coupled dynamics of fluid flow, heat transfer, mass transport, and electrochemistry, addressing significant challenges in predicting the interactions between molten salts and structural materials. The implementation of a modified interface current enables the simulation of both electrochemical kinetics and mass transfer effects, overcoming previous modeling limitations. Our findings demonstrate the critical role of redox states and temperature gradients in influencing corrosion rates of structural alloys, such as nickel-chromium-molybdenum alloys, and the dynamics of noble metal deposition. The simulations reveal how localized hydrodynamic conditions enhance mass transfer, affecting the distribution of corrosion products and noble metals. This work provides vital insights into material behavior under operational conditions, informing strategies for optimizing reactor design and operational safety.

## SUMMARY

This report study dynamics of corrosion mechanisms and noble metal plating behaviors in molten salt reactors (MSRs), leveraging advanced multiphysics modeling techniques through the MOOSE framework. The research builds upon the existing integrated Poisson-Nernst-Planck (PNP) model developed in FY24, enhancing its capabilities to capture the coupled interactions of fluid flow, heat transfer, mass transport, and electrochemical processes.

One of the central advancements of this study is the implementation of a modified interface current, which integrates the simulation of electrochemical kinetics with mass transfer effects. This development addresses critical limitations of prior models, enabling a more accurate representation of the interactions between molten salts and structural materials.

The findings underscore the significant influence of redox states and temperature gradients on the corrosion rates of structural alloys, particularly stainless steel alloys, which are commonly used in reactor construction. The study illustrates how localized hydrodynamic conditions, driven by flow dynamics and thermal buoyancy, enhance mass transfer processes, subsequently impacting the distribution and behavior of corrosion products and noble metals within the reactor environment.

Moreover, the simulations show that variations in temperature and chemical composition within the reactor can lead to differential corrosion rates and noble metal deposition patterns. These insights are key for understanding the long-term stability and integrity of materials used in MSRs, as they highlight the necessity of managing both chemical composition and flow dynamics to optimize reactor performance and mitigate corrosion risks.

This work provides knowledge on the material behavior under operational conditions in MSRs, offering guidance for the development of strategies aimed at enhancing reactor design, improving operational safety, and extending the lifespan of critical structural components. The research contributes to the growing body of knowledge necessary for advancing molten salt reactor technology and ensuring the successful deployment of this energy solution.

## **ACKNOWLEDGMENTS**

This report was authored by a contractor of the U.S. Government under Contract DE-AC07-05ID14517. Accordingly, the U.S. Government retains a non-exclusive, royalty-free license to publish or reproduce the published form of this contribution or to allow others to do so for U.S. Government purposes. Funding was provided by the Nuclear Energy Advanced Modeling and Simulation program.

This research made use of the resources of the High Performance Computing Center at Idaho National Laboratory, which is supported by the Office of Nuclear Energy of the U.S. Department of Energy and the Nuclear Science User Facilities under Contract No. DE-AC07-05ID14517.

*Page intentionally left blank*

# CONTENTS

ABSTRACT	iii
SUMMARY	iv
ACKNOWLEDGMENTS	v
ACRONYMS	x
1. INTRODUCTION	1
2. CORROSION AND NOBLE-METAL PLATING IN MOLTEN SALTS: TRANSPORT PHENOMENA AND MODELING RATIONALE FOR A PNP FRAMEWORK	3
2.1. Phenomenology Description . . . . .	3
2.2. Species-transport mechanisms relevant to noble metals and corrosion products . . . . .	3
2.3. Experimental and modeling baselines . . . . .	4
2.4. Why a Poisson-Nernst-Planck (PNP) core with a modified interface current? . . . . .	4
2.5. Scope for the PNP section that follows . . . . .	5
3. POISSON–NERNST–PLANCK FORMULATION FOR MOLTEN-SALT REACTOR CHEMISTRY	6
3.1. Liquid domain $\Omega_\ell$ : RANS–PNP system . . . . .	6
3.2. Solid domain $\Omega_s$ : electronic conduction, heat conduction, and (optional) solid chemistry . . . . .	7
3.3. Boundary and initial conditions (without interfacial current) . . . . .	8
3.4. Modeling notes specific to molten salts . . . . .	8
4. FORMULATION OF A MASS AND ELECTRO-CHEMISTRY TRANSPORT CONSISTENT INTERFACE CURRENT	9
4.1. Formulation of the mass-transfer model and analysis via correlations or computed friction factors . . . . .	9
4.1.1. Correlation for internal flows . . . . .	9
4.1.2. Improved Wall-Resolved Friction Factor via Chilton–Colburn Formulation . . . . .	10
4.1.3. Local vs. bulk, transitional blending, and development. . . . .	10
4.1.4. Coupling to the species equation and PNP consistency. . . . .	10
4.2. Butler–Volmer electro-kinetics and interpretation . . . . .	11
4.2.1. Butler–Volmer rate law (kinetic control). . . . .	11
4.2.2. Physical interpretation. . . . .	12
4.2.3. Consistency with PNP and thermochemistry. . . . .	12
4.2.4. Dimensional and sign checks. . . . .	12
4.3. Two-film formulation and derivation of the interfacial current . . . . .	12
4.3.1. Liquid film transport with migration. . . . .	13
4.3.2. Faradaic stoichiometry at the interface. . . . .	13
4.3.3. Coupling to Butler–Volmer and elimination of $c_w$ . . . . .	14
4.3.4. Analysis: limiting currents and asymptotic regimes. . . . .	14
4.3.5. Generalization to multi-species stoichiometry. . . . .	15
4.3.6. Remarks on consistency with PNP and numerical coupling. . . . .	15
4.4. Interpretation of the derived current and details on the numerical implementation . . . . .	16

5.	DEMONSTRATION FOR THE LOTUS MOLTEN SALT REACTOR	18
5.1.	Simulation setup for the open-source MCREE demonstration case . . . . .	18
5.2.	Thermochemical phenomena demonstrated by the open-source MCREE case . . . . .	20
5.3.	Description of results . . . . .	22
6.	CONCLUSIONS AND FUTURE WORK	29
7.	REFERENCES	31

## FIGURES

Figure 1.	Flow streamlines colored with the fuel salt temperature field in the reactor core and the temperature field in the reactor vessel and reflector. The contours showcase the temperature profiles obtained within the reactor core, which govern the mass transport processes. . . . .	23
Figure 2.	Flow streamlines around the inlet recirculation zone colored with the angular velocity and the temperature field in the reactor vessel and reflector. The figure showcases the detachment of the boundary layer at the reactor inlet, which results on a large friction factor before the tripping point and significant mass transfer in that region. . . . .	24
Figure 3.	Distribution of corrosion species in the reactor core and reactor vessel between the reactor and the neutron reflector after 10,000,000 seconds ( $\sim 115.7$ days) of operation. . . . .	25
Figure 4.	Distribution of plating species in the reactor core and reactor vessel between the reactor and the neutron reflector after 10,000,000 seconds ( $\sim 115.7$ days) of operation. . . . .	26
Figure 5.	Evolution of Cr during operation transient. The evolution showcases a fast initial buildup with a corrosion rate stopping at later stages as free Chlorine is reduced by the corrosion products. <i>Note:</i> to display the animation Adobe Acrobat Reader or a similar viewing tool with animation capabilities is required. . . . .	27
Figure 6.	Evolution of Ru during operation transient. The evolution showcases a liquid distribution reaching equilibrium, while the plated ruthenium builds up in the reactor vessel around the code. <i>Note:</i> to display the animation Adobe Acrobat Reader or a similar viewing tool with animation capabilities is required. . . . .	28

## TABLES

Table 1.	Modeled operating conditions and key parameters used in the MCREE case. . . . .	19
----------	---	----

*Page intentionally left blank*

## ACRONYMS

<b>CFD</b>	Computational Fluid Dynamics
<b>INL</b>	Idaho National Laboratory
<b>MCRE</b>	Molten Chloride Reactor Experiment
<b>MOOSE</b>	Multiphysics Object-Oriented Simulation Environment
<b>MSR</b>	Molten Salt Reactor
<b>MSRE</b>	molten salt reactor experiment
<b>PNP</b>	Poisson–Nernst–Planck

*Page intentionally left blank*

# **Complete Pronghorn Electrochemistry Modeling Improvements for Corrosion and Plating Modeling**

## **M3 Milestone Report**

### **1. INTRODUCTION**

The emerging Molten Salt Reactor (MSR) technology represents a significant shift in nuclear energy paradigms, promising improvements in safety, efficiency, and sustainability. MSRs utilize molten salts, primarily composed of fluoride or chloride compounds, as both coolant and fuel, allowing for operation at elevated temperatures while maintaining low pressures. This not only enhances thermal efficiency but also reduces the risk of catastrophic failure scenarios associated with traditional water-cooled reactors. However, the unique operational environment of MSRs introduces complex interactions between the molten salts and structural materials that pose significant challenges, particularly concerning corrosion and noble metal plating.

Corrosion of structural alloys, such as stainless steels or high-performance nickel-chromium-molybdenum alloys (e.g., Hastelloy N), is a critical area of concern in the design and operation of MSRs. Experimental studies have shown that the corrosion behavior of these alloys is influenced by several factors, including the redox state of the salt, temperature gradients, and impurity levels. Decades of experience, especially from the Oak Ridge National Laboratory (ORNL) with the Aircraft Reactor Experiment (ARE) and the molten salt reactor experiment (MSRE), have established that while uniform corrosion can be minimized through meticulous control of these parameters, localized corrosion phenomena can still arise. For instance, tellurium-induced embrittlement and chromium dealloying have been observed under certain conditions, leading to significant reductions in material integrity and potential failure modes.

Concurrent with corrosion concerns, the behavior of noble metals generated as fission products, particularly ruthenium, rhodium, palladium, and silver, presents additional challenges in molten salt environments. These noble metals tend to migrate within the salt and deposit on reactor surfaces, which can adversely affect reactor performance and longevity and generate a re-distribution of the decay heat in the reactor core. Laboratory investigations have demonstrated that the transport and deposition of noble metals are influenced by a range of factors, including temperature gradients (thermophoresis), turbulence-driven dispersion, and surface interactions with reactor materials. The complex interplay of these variables necessitates a deep understanding of the transport phenomena governing noble metal behavior.

Historically, researchers have approached the modeling of corrosion and noble metal plating with a variety of methods, often relying on simplified models that treat these phenomena separately. While some studies have employed empirical correlations or focused on specific aspects of mass transfer and electrochemical kinetics, there remains a significant gap in integrated modeling approaches that capture the multifaceted nature of these processes in a cohesive framework. The limitations of traditional modeling techniques underscore the need for advanced simulation tools that can account for the coupled dynamics of fluid flow, heat transfer, mass transport, and electrochemistry.

The Multiphysics Object-Oriented Simulation Environment (MOOSE) framework offers a powerful solution to this challenge by enabling the development of coupled multiphysics models that can simulate the complex interactions within MSR systems. MOOSE facilitates the integration of various physical processes, including Computational Fluid Dynamics (CFD), thermochemistry, and electrochemical kinetics, allowing for a more comprehensive analysis of how these factors influence corrosion and noble metal plating. By utilizing MOOSE applications, one can develop robust simulations that reflect the realistic operating conditions of MSRs and provide valuable insights into material behavior.

In FY24, an original implementation of the Poisson–Nernst–Planck (PNP) model was developed in the MOOSE framework [1]. This model used a Butler–Volmer interface condition to model chemical kinetics at the interface. Although this model proved efficient in modeling electro-galvanic corrosion in laminar flow loops, it presented a few shortcomings:

1. The model did not consider mass transfer mechanisms in the fluid, which determine the concentration of corrosion products next to the wall and hence, define the corrosion rates,
2. The model assumed the concentration of the cathodes in the first cell near the wall as the bulk concentration that was used for the cathodic exchange current, which lead to an over-estimation of the concentration of the cathodes participating in the exchange current and hence the need to significantly refine the computational mesh to avoid artificially reducing the corrosion rates,
3. The model did not consider the gradients of the chemical potential as a driving force in corrosion, which lead to an under-estimation of the corrosion rates in regions of large chemical potential gradients such as elbows or flow detachment regions,
4. The electrochemistry-only nature of the model developed could not model exchange phenomena governed by non-electrochemical phenomena, such as noble metal plating.

In this report, we discuss the improvements in the PNP model and the interface exchange current to overcome the previous limitations in the model. We focus on the mechanisms by which fission products and corrosion products interact with structural materials, employing a PNP framework coupled with CFD to model these processes. This re-evaluation leads to the integration of chemical potential gradients in the diffusion current in the PNP model and the development of an interface current that integrate both the mass and electrochemistry transport effects. Through simulations, we investigate the effects of temperature distribution, flow dynamics, and chemical interactions on the distribution and behavior of corrosion and noble metal species in an example case of an open source version of the Molten Chloride Reactor Experiment (MCRE).

Our study includes a rigorous examination of the evolution of corrosion species, such as chromium, and noble metals, such as ruthenium, over extended operational periods. By analyzing the underlying thermochemical interactions and mass transfer dynamics, we provide insights into the factors that govern material integrity and performance in MSR environments. The findings of this research not only enhance our understanding of corrosion and noble metal behavior in molten salts but also inform the development of strategies to mitigate these issues, ultimately contributing to the safe and efficient operation of future nuclear reactors.

## 2. CORROSION AND NOBLE-METAL PLATING IN MOLTEN SALTS: TRANSPORT PHENOMENA AND MODELING RATIONALE FOR A PNP FRAMEWORK

MSRs and molten-salt heat-transfer systems exhibit a coupled set of electrochemical, thermochemical, and hydrodynamic phenomena governing alloy corrosion and the transport, agglomeration, and plating of noble-metal fission products (notably Ru, Rh, and Ag) and corrosion products (e.g., Cr, Ni, Fe halides) [2–5]. Decades of ORNL experience (ARE/MSRE) established that fluoride salts can be operated with low uniform corrosion when salt redox potential is controlled and impurities are minimized; nonetheless, localized phenomena—such as tellurium-induced embrittlement, chromium dealloying, and noble-metal plate-out—produce system-level signatures that must be modeled mechanistically [6–9].

### 2.1. Phenomenology Description

In fuel-bearing fluoride salts (e.g., FLiBe), most fission products form soluble fluorides (*salt-seekers*), whereas a subset (“noble metals”) forms metallic particles or colloids with negligible fluoride stability and limited wetting of salt, tending to migrate and deposit on metal/graphite and salt-gas interfaces [6, 7, 10, 11]. MSRE analyses and recent laboratory studies indicate that Ru and Rh are dominantly metallic and accumulate on cold surfaces, pump bowls, and within off-gas trains; Ag behaves semi-noble in fluorides (it may form AgF under some conditions), but it was grouped with noble/semi-noble species in MSRE deposits and shows surface affinity and aerosol entrainment pathways relevant to modern MSR designs [7, 12–14]. Noble-metal transport shows strong sensitivity to temperature gradients (thermophoresis), turbulence-driven dispersion, interfacial area exposure (sparging), and surface chemistry (oxide/fluoride films, graphite) [6, 10, 15].

Corrosion of Ni–Cr–Mo alloys (e.g., Hastelloy N) in purified fluoride salts is primarily driven by redox-mediated dissolution of the least noble constituent (Cr) and by impurity spikes (HF, metal fluorides), with dissolution products transported as soluble halides and subsequently redeposited (often as metallic Ni/Fe) where the local chemical potential and temperature favor reduction [3, 16–18]. When tellurium is present from fission, grain-boundary attack and embrittlement can occur despite otherwise low uniform corrosion [8, 9, 19]. Modern datasets synthesize thousands of measurements across salts and alloys and confirm (i) strong dependence on salt purity/redox, (ii) diffusion-migration control for dissolved species, and (iii) flow and surface-chemistry control for particles/colloids [3, 20, 21].

### 2.2. Species-transport mechanisms relevant to noble metals and corrosion products

The governing transport of dissolved ions in molten salts combines advection, Fickian diffusion, and electromigration, with temperature- and composition-dependent diffusivities and mobilities [3, 22, 23]. For metallic fission products (Ru, Rh, Ag) born *in situ*, pathways include: (1) nucleation to nanometer-scale particles; (2) Brownian and turbulence-enhanced transport; (3) capture at solid interfaces (metals, graphite) with attachment kinetics governed by interfacial energetics and local electrochemical potential; (4) entrainment to off-gas as mist/aerosol from gas-salt interfaces [6, 7, 10, 14, 15]. Graphite and alloy surfaces differ markedly in adhesion and retention behavior; experiments with FLiBe/FLiNaK show stronger deposition on Ni-rich alloys than on graphite for several noble metals (including Ru and Rh), and sensitivity of Mo-like species to salt redox [6, 7, 12].

For corrosion products, chromium dissolves as  $\text{CrF}_x^{(3-x)-}$  (effective charge depends on complex specia-

tion), migrates with the ionic current, and can redeposit as metallic Cr under reducing conditions, establishing source-sink loops that couple walls, bulk salt, and cold traps [3, 5, 16, 17]. Local electric fields arise from galvanic patches, composition gradients, and mixed-conductor films, further biasing ionic fluxes [24, 25].

### 2.3. Experimental and modeling baselines

ORNL reports correlated noble-metal distributions with mass-transfer theory and operational transients, identifying strong plate-out at the pump bowl and heat exchanger and salt-gas regions; Ru/Rh-rich deposits were confirmed by gamma spectrometry and remote assay [2, 6, 7, 26].

Meta-analyses across fluoride and chloride salts quantify corrosion versus salt purity/redox and alloy chemistry, while targeted electrochemical experiments (e.g., potentiodynamic/potentiostatic chromium dissolution in FLiNaK) reveal transitions between charge-transfer and diffusion-limited regimes [3, 20, 27]. Dealloying morphologies and potential-dependent kinetics (Ni–Cr, Alloy 625) observed at 600–700 °C directly inform reaction-transport closures [19, 28]. For noble metals, recent FLiBe studies (Ru, Rh, Mo, Te) measured partitioning between salt, graphite, and Ni-rich alloys and demonstrated redox sensitivity and flow-driven re-suspension [10, 12]. Off-gassing studies detail aerosol capture requirements and mists formed at sparge interfaces, a key removal/control pathway for noble metals [14, 15, 29].

Pyroprocessing in LiCl–KCl consistently shows noble-metal retention as refractory metallic residues and informs particle-scale transport/aggregation models (nucleation, coalescence, settling) transferable to MSR source-term modeling, albeit with different solvent chemistry [30, 31]. Thermal salt loops for CSP reinforce the primacy of purity and redox control for corrosion mitigation and provide flow/thermal datasets useful for validating mixed advection-diffusion-reaction closures in halide melts [4, 32].

### 2.4. Why a Poisson-Nernst-Planck (PNP) core with a modified interface current?

Dissolved ionic species ( $\text{UF}_{4/3}$ , corrosion halides, redox buffers) respond to gradients of concentration, potential, and temperature. A PNP core self-consistently couples:

$$\partial_t c_i + \nabla \cdot (\mathbf{u} c_i - D_i \nabla c_i - z_i u_i c_i \nabla \phi) = R_i(c, \phi, T), \quad -\nabla \cdot (\varepsilon \nabla \phi) = \rho_f + \sum_i z_i e c_i,$$

closing with temperature- and composition-dependent  $D_i$ , mobilities  $u_i$ , and reaction terms  $R_i$  drawn from thermochemical data [22, 24, 25]. This framework naturally represents redox control (e.g.,  $\text{UF}_4/\text{UF}_3$ , Be additions), mixed-potential environments, and electromigration of charged corrosion products [3–5].

What PNP does *not* directly capture are (i) neutral metallic particles (Ru/Rh/Ag) and (ii) attachment/detachment at rough, reactive walls. We therefore augment the standard Butler-Volmer interfacial flux with a *modified interface current* comprising:

1. an electrochemical term  $j_{\text{BV}}(\eta, c_i, T)$  for electron-transfer-limited dissolution/precipitation of ionic metal halides;
2. a particle-capture term  $j_{\text{cap}} = \kappa_{\text{geom}} \alpha(T, \phi) c_p \mathcal{F}(\text{Shear, wetting})$  for metallic Ru/Rh/Ag clusters, where  $c_p$  is particle concentration,  $\alpha$  encodes sticking vs. re-entrainment, and  $\kappa_{\text{geom}}$  resolves local roughness/porosity;

3. a nucleation source  $S_p(c_i, \phi, T)$  that converts dissolved precursors into neutral clusters when supersaturation exceeds a critical value (optionally via classical nucleation or data-driven closures).

Evidence supporting this split comes from MSRE mass-transfer reconciliations, aerosol/plate-out in off-gas systems, and recent PNP-based, flow-informed corrosion models showing agreement with loop experiments and highlighting the role of electromigration and local overpotentials under high-temperature conditions [6, 10, 13, 14, 33]. For tellurium effects, we retain a separate grain-boundary damage metric driven by local Te activity and exposure time, decoupled from PNP but coupled to wall chemistry [8, 19].

The following targets are identified for model-data alignment targets:

1. *Noble metals*: reproduce Ru/Rh plate-out fractions and spatial patterns (pump bowl, heat exchangers, sparge interfaces) under MSRE-like flow and redox; sensitivity to sparge rate and thermal boundary conditions [6, 7, 10, 15].
2. *Corrosion*: match Cr loss rates vs. redox/purity; predict re-deposition signatures (Fe/Ni) and dealloying morphologies; capture transitions between activation- and diffusion-limited regimes [3, 16, 17, 28].
3. *System response*: quantify off-gas loading (aerosolized noble metals), cold-leg deposition, and particle resuspension thresholds; propagate to source-term and maintenance planning [14, 29, 34].

## 2.5. Scope for the PNP section that follows

The PNP formulation with a modified interface current is therefore well-motivated: it delivers a single, physics-grounded backbone for dissolved-species transport and electrochemistry, while incorporating particle capture/nucleation for Ru/Rh/Ag and data-validated wall laws for corrosion and redeposition. The same framework can be exercised against legacy MSRE data, modern loop experiments (FLiNaK/FLiBe), and cross-domain pyroprocessing observations to reduce uncertainty in mechanistic source terms relevant to licensing and design [3, 6, 10, 20, 33].

**Notes on data gaps.** Silver behavior in fluorides shows chemistry-dependent partitioning (AgF stability vs. semi-noble plate-out); we adopt the conservative noble/semi-noble treatment consistent with MSRE groupings and modern off-gas/aerosol evidence, and recommend targeted Ag partitioning tests under intended redox/purity envelopes [7, 14, 15].

### 3. POISSON–NERNST–PLANCK FORMULATION FOR MOLTEN-SALT REACTOR CHEMISTRY

We present a complete Poisson–Nernst–Planck (PNP) model for multicomponent molten salts appropriate to liquid-fueled reactor conditions. The formulation is posed on two disjoint domains: the liquid electrolyte domain  $\Omega_\ell$  (the circulating salt) and the solid, electronically conducting domain  $\Omega_s$  (structural alloy, electrodes, or current collectors). Interfacial source terms and current closure at  $\Gamma = \partial\Omega_\ell \cap \partial\Omega_s$  are deferred to a subsequent section; here, each domain is closed internally. The model is written on a *molar basis* with species concentrations  $c_i$  in  $\text{mol m}^{-3}$  and electrostatic potentials in volts.

#### Unknown fields, constitutive closures, and conventions

In the liquid  $\Omega_\ell$  we solve for the mean velocity  $\mathbf{u}$ , pressure  $p$ , temperature  $T$ , electrostatic potential  $\phi_\ell$ , and the molar concentrations  $\{c_i\}_{i=1}^{N_s}$  of mobile ionic species (e.g.,  $\text{Li}^+$ ,  $\text{F}^-$ , actinide and fission-product complexes). Turbulence is represented by a RANS eddy viscosity  $\mu_t$  and associated scalar eddy diffusivities; unless otherwise stated, the Boussinesq approximation is used for buoyancy. In the solid  $\Omega_s$  we solve for the electronic potential  $\phi_s$ , temperature  $T_s$ , and (optionally) diffusing alloying elements  $w_j$  if solid-state chemistry is of interest. Interfaces, electrochemical currents, and plating/corrosion fluxes are *not* imposed here.

The ionic flux model is the generalized Nernst–Planck law derived from a nonequilibrium chemical potential  $\mu_i = \mu_i^\circ + RT \ln a_i + z_i F \phi_\ell$ , with activity  $a_i = \gamma_i c_i / c^\circ$ :

$$\mathbf{J}_i^{\text{NP}} = -D_i \left( \nabla c_i + c_i \nabla \ln \gamma_i + \frac{z_i F}{RT} c_i \nabla \phi_\ell \right), \quad D_i = D_i(T) (> 0). \quad (1)$$

Nonideality enters through  $\gamma_i(T, \{c_k\}, \xi)$ , which may be supplied by a thermochemical solver (e.g. Thermochimica) or a fitted activity model. Turbulence augments molecular diffusion through a gradient-diffusion closure with turbulent Schmidt number  $\text{Sc}_{t,i}$ :

$$D_{i,\text{eff}} = D_i + D_{t,i}, \quad D_{t,i} = \frac{\mu_t}{\rho \text{Sc}_{t,i}}, \quad \text{Sc}_{t,i} \approx 0.7–1.0 \text{ (unless calibrated)}. \quad (2)$$

Analogously, the effective thermal conductivity is  $k_{\text{eff}} = \lambda + \rho c_p \mu_t / \text{Pr}_t$  with  $\text{Pr}_t \simeq 0.85–0.9$  for molten salts. The free charge density is  $\rho_e = F \sum_i z_i c_i + \rho_{\text{fixed}}$ , where  $\rho_{\text{fixed}}$  accounts for any immobile background charge (often zero in homogeneous liquids).

#### 3.1. Liquid domain $\Omega_\ell$ : RANS–PNP system

The liquid is modeled as a conducting, incompressible mixture, with density variations only in the buoyancy term (Boussinesq). The governing equations for mass, momentum, energy, electrostatics, and

species are:

$$\nabla \cdot \mathbf{u} = 0, \quad (3)$$

$$\rho(\partial_t \mathbf{u} + \mathbf{u} \cdot \nabla \mathbf{u}) = -\nabla p + \nabla \cdot [\mu_{\text{eff}}(\nabla \mathbf{u} + (\nabla \mathbf{u})^\top)] + \rho \mathbf{g} - \rho_0 \beta(T - T_0) \mathbf{g} + \rho_e \mathbf{E}, \quad (4)$$

$$\rho c_p(\partial_t T + \mathbf{u} \cdot \nabla T) = \nabla \cdot (k_{\text{eff}} \nabla T) + q_J + q_{\text{chem}}, \quad (5)$$

$$-\nabla \cdot (\epsilon_\ell \nabla \phi_\ell) = \rho_e \equiv F \sum_{i=1}^{N_s} z_i c_i + \rho_{\text{fixed}}, \quad (6)$$

$$\partial_t c_i + \nabla \cdot (c_i \mathbf{u} + \mathbf{J}_i) = R_i, \quad \mathbf{J}_i = -D_{i,\text{eff}} \left( \nabla c_i + c_i \nabla \ln \gamma_i + \frac{z_i F}{RT} c_i \nabla \phi_\ell \right), \quad (7)$$

where  $\mu_{\text{eff}} = \mu + \mu_t$  and  $\mathbf{E} = -\nabla \phi_\ell$ . The Joule heating  $q_J$  uses the *conduction* current density  $\mathbf{i}_{\text{cond}}$  (see below) as  $q_J = \mathbf{i}_{\text{cond}} \cdot \mathbf{E}$ . The source term  $q_{\text{chem}}$  accounts for homogeneous reactions/solvation heat if modeled;  $R_i$  collects homogeneous production/consumption of species  $i$  (e.g., redox buffering). Turbulence may be represented by a standard or low-Re  $k-\epsilon$  closure to determine  $\mu_t$ ; the buoyancy production  $G_b = \rho \mu_t (\mathbf{g} \cdot \nabla T) / \Pr$  and any re-laminarization damping act only through  $\mu_t$ ,  $D_{t,i}$ , and  $k_{\text{eff}}$  in (4)–(7).

The total current density carried by ions is

$$\mathbf{i} = F \sum_i z_i (\mathbf{J}_i + c_i \mathbf{u}) = \underbrace{\left[ -\frac{F^2}{RT} \sum_i z_i^2 D_{i,\text{eff}} c_i \nabla \phi_\ell - F \sum_i z_i D_{i,\text{eff}} (\nabla c_i + c_i \nabla \ln \gamma_i) \right]}_{\mathbf{i}_{\text{cond}}} + \rho_e \mathbf{u}. \quad (8)$$

The bracketed term is the *conduction* current  $\mathbf{i}_{\text{cond}}$  that produces Joule heat  $q_J = \mathbf{i}_{\text{cond}} \cdot \mathbf{E}$ ; the convective part  $\rho_e \mathbf{u}$  does not dissipate. In quasi-uniform electrolytes where composition gradients are weak, one may define a local effective conductivity

$$\sigma_{\text{eff}} \equiv \frac{F^2}{RT} \sum_i z_i^2 D_{i,\text{eff}} c_i, \quad \text{so that} \quad \mathbf{i}_{\text{cond}} \approx -\sigma_{\text{eff}} \nabla \phi_\ell. \quad (9)$$

Equations (6) and (7) together enforce charge conservation,  $\partial_t \rho_e + \nabla \cdot \mathbf{i} = 0$ .

Under MSR conditions the ionic strength is high and deviations from ideality are significant. The activity gradient  $c_i \nabla \ln \gamma_i$  in (1) is required for thermodynamic consistency of species diffusion. If a mobility model is preferred, the electromigration term may be written as  $z_i F c_i \mathbf{u}_i^{\text{el}}$  with  $\mathbf{u}_i^{\text{el}} = (D_{i,\text{eff}} / RT) \mathbf{E}$ . Maxwell–Stefan diffusion can be used as an alternative to (1); here we retain the PNP form with activity correction because it integrates cleanly with (6).

Away from charged interfaces the Debye length  $\lambda_D = \sqrt{\epsilon_\ell RT / (F^2 \sum_i z_i^2 c_i)}$  is typically much smaller than geometric scales. In that limit  $\sum_i z_i c_i + \rho_{\text{fixed}} / F \approx 0$  and (6) reduces to a constraint eliminating rapid space-charge oscillations. We keep the full Poisson equation to remain valid in thin layers and under transients; the electroneutral approximation is a controlled simplification for diagnostics.

### 3.2. Solid domain $\Omega_s$ : electronic conduction, heat conduction, and (optional) solid chemistry

In metals and electronically conducting solids the mobile ionic species are negligible and the electron gas screens charge over atomic scales. The electrostatic field is governed by charge conservation under Ohm's

law:

$$\nabla \cdot (\sigma_s \nabla \phi_s) = 0, \quad \mathbf{i}_s = -\sigma_s \nabla \phi_s, \quad q_{J,s} = \sigma_s |\nabla \phi_s|^2, \quad (10)$$

with  $\sigma_s(T_s, \mathbf{x})$  the solid electrical conductivity. Because free charge is screened, the Poisson equation reduces to Laplace's equation for  $\phi_s$ ;  $\epsilon_s$  appears only in capacitive transients not resolved here.

The solid energy equation is a Fourier heat balance with ohmic heating and, if desired, latent/source terms due to microchemistry:

$$\rho_s c_{p,s} \partial_t T_s = \nabla \cdot (\lambda_s \nabla T_s) + q_{J,s} + q_{\text{chem},s}. \quad (11)$$

If redistribution of alloying elements is modeled (e.g., Cr, Fe, Ni in austenitic steels), one solves Fickian diffusion with possible cross-effects (thermodiffusion, electromigration) if currents are large:

$$\partial_t w_j = \nabla \cdot \left( D_j^{(s)} \nabla w_j \right) + R_j^{(s)}, \quad j \in \{\text{Cr, Fe, Ni, ...}\}, \quad (12)$$

where  $w_j$  is a mass (or molar) fraction in the solid and  $R_j^{(s)}$  collects precipitation or phase-change kinetics if included. Electromigration of solutes in metals is typically small at reactor-relevant current densities and is omitted here; it can be added as a drift term proportional to  $\nabla \phi_s$  if needed.

### 3.3. Boundary and initial conditions (without interfacial current)

Because interfacial electrochemistry is reserved for a later section, we outline only physically neutral conditions that close each domain independently. In the liquid, no-slip and impermeable walls impose  $\mathbf{u} = \mathbf{0}$  and  $\mathbf{n} \cdot \mathbf{J}_i = 0$  on solid boundaries not used for chemistry; thermal walls are either isothermal  $T = T_w$  or adiabatic  $\mathbf{n} \cdot (k_{\text{eff}} \nabla T) = 0$ . Electrostatic walls are insulating,  $\mathbf{n} \cdot (\epsilon_\ell \nabla \phi_\ell) = 0$ , unless a prescribed potential or field is applied. Inlets use specified  $(\mathbf{u}, T, \{c_i\})$  and outlets employ standard do-nothing/traction-free conditions consistent with (4)–(7). In the solid, one prescribes either  $\phi_s$  or  $\mathbf{n} \cdot \mathbf{i}_s$  on boundaries that will eventually connect to an electrochemical interface; for the present section, homogeneous Neumann  $\mathbf{n} \cdot \mathbf{i}_s = 0$  suffices. Thermal boundary conditions mirror the liquid side (continuity of temperature and heat flux will be enforced at  $\Gamma$  once coupling is activated). Initial conditions specify  $(\mathbf{u}, T, \phi_\ell, \{c_i\})$  in  $\Omega_\ell$  and  $(T_s, \phi_s)$  in  $\Omega_s$ .

### 3.4. Modeling notes specific to molten salts

Molten fluoride and chloride salts are concentrated electrolytes; activities  $\gamma_i$  and transport coefficients  $D_i$  are strongly temperature- and composition-dependent. The activity term  $c_i \nabla \ln \gamma_i$  in (1) is essential to obtain physically consistent diffusion and to couple seamlessly with thermochemical equilibrium calculations. The effective conductivity (9) often varies by orders of magnitude across the core and must be evaluated locally from the evolving  $\{c_i\}$  and  $T$ . Turbulence affects electrodifusion primarily through  $D_{t,i}$  and  $k_{\text{eff}}$ ; the electric body force  $\rho_e \mathbf{E}$  in (4) is normally confined to thin space-charge layers and can be neglected in core-averaged balances, but it is retained here for completeness and to accommodate electroosmotic phenomena in confined passages. Finally, although the electroneutral limit is appropriate in most of the bulk, keeping the full Poisson equation ensures that near-wall double layers, polarization under strong transients, and regions with large composition gradients are treated without additional assumptions.

Equations (3)–(7) in  $\Omega_\ell$  together with (10)–(12) in  $\Omega_s$  define the complete PNP framework used here for molten-salt reactor chemistry. Interfacial fluxes and current continuity at  $\Gamma$  will be introduced in Sec. 4.1., where the electrochemical kinetics, charge balance, and mass-transfer limitations at the liquid–solid boundary are enforced.

## 4. FORMULATION OF A MASS AND ELECTRO-CHEMISTRY TRANSPORT CONSISTENT INTERFACE CURRENT

### 4.1. Formulation of the mass–transfer model and analysis via correlations or computed friction factors

We begin with the liquid–side transport of each electroactive ionic species  $i$  in the near–wall region adjacent to the metal surface. Throughout we work on a molar basis, with  $c_i$  in  $\text{mol m}^{-3}$  and fluxes in  $\text{mol m}^{-2} \text{s}^{-1}$ . In the spirit of two–film theory, the net interfacial molar flux on the liquid side is modeled as a first–order “film” law

$$J_{i,\ell} = k_{m,i} (c_{i,b} - c_{i,w}), \quad k_{m,i} = \frac{\text{Sh}_i D_i}{d_h}, \quad (13)$$

where  $c_{i,b}$  and  $c_{i,w}$  are, respectively, a near–wall bulk value (taken as the solution value at the first off–wall point) and the liquid–side interfacial value at the wall,  $D_i(T)$  is the molecular diffusivity,  $d_h$  is a characteristic hydraulic length (e.g. channel hydraulic diameter), and  $\text{Sh}_i$  is the Sherwood number. The coefficient  $k_{m,i}$  is species–dependent through  $D_i$  and  $\text{Sc}_i = \nu/D_i$ , and it inherits the local hydrodynamics through  $\text{Re}$ , the friction velocity  $u_*$ , and the wall shear stress  $\tau_w = \rho u_*^2$ . In the RANS–PNP model of Sec. 3., the turbulent eddy viscosity  $\mu_t$  modifies near–wall scalar transport; the film coefficient captures the resultant, composite transfer across the concentration sublayer and is the quantity that couples to interfacial electrochemistry in later subsections.

Two complementary routes are used to evaluate  $k_{m,i}$ . In the *correlation route*,  $\text{Sh}_i$  is obtained from canonical internal–flow correlations parameterized by  $\text{Re}$  and  $\text{Sc}_i$ , with standard developing–length and property–variation corrections. In the *friction–factor route*, we compute a local mass–transfer j–factor from the wall shear (or friction factor) produced by the CFD solution and obtain  $\text{Sh}_i$  via the Chilton–Colburn analogy; this route automatically embeds buoyancy and re–laminarization effects through the predicted  $u_*$  and  $C_f$ .

#### 4.1.1. Correlation for internal flows

For fully developed, *laminar* flow with constant wall concentration in circular passages,  $\text{Sh}_i = 3.66$ . In developing laminar flow, the Leveque/Sieder–Tate form applies,

$$\text{Sh}_i = 1.62 \left( \text{Re} \text{Sc}_i \frac{d_h}{x} \right)^{1/3} \quad (\text{entry region}), \quad (14)$$

$$\text{Sh}_i = 3.66 + 0.065 \frac{\text{Re} \text{Sc}_i d_h}{L} / \left[ 1 + 0.04 \left( \text{Re} \text{Sc}_i d_h / L \right)^{2/3} \right] \quad (\text{finite } L), \quad (15)$$

with  $x$  the axial distance from the inlet and  $L$  the characteristic development length. For *turbulent* internal flow, the Gnielinski–type correlation for mass transfer reads

$$\text{Sh}_i = \frac{\frac{f_D}{8} (\text{Re} - 1000) \text{Sc}_i}{1 + 12.7 \left( \frac{f_D}{8} \right)^{1/2} \left( \text{Sc}_i^{2/3} - 1 \right)}, \quad 10^4 \lesssim \text{Re} \lesssim 10^6, \quad 0.6 \lesssim \text{Sc}_i \lesssim 3000, \quad (16)$$

where  $f_D$  is the Darcy friction factor. For smooth pipes,  $f_D$  may be given by Blasius  $f_D = 0.316 \text{Re}^{-1/4}$  in the range  $3 \times 10^3 \lesssim \text{Re} \lesssim 10^5$ , or by Petukhov/Colebrook forms if roughness or a wider Reynolds range must be covered. In molten salts  $\text{Sc}_i = \nu/D_i$  is typically large ( $\mathcal{O}(10^2 - 10^3)$ ), so the  $\text{Sc}_i^{2/3}$  term

controls the denominator in (16); this results in  $\text{Sh}_i \sim (\frac{f_D}{8}) \text{Re} \text{Sc}_i^{1/3}$  to leading order, consistent with the  $j$ -factor analogy below. Property–variation effects can be included with a weak Sieder–Tate–type correction,  $\text{Sh}_i \rightarrow \text{Sh}_i(\mu/\mu_w)^{0.14}$  or  $\text{Sh}_i \rightarrow \text{Sh}_i(\text{Sc}_i/\text{Sc}_{i,w})^{0.14}$ , when the wall-to-bulk viscosity or diffusivity ratios deviate appreciably from unity.

#### 4.1.2. Improved Wall-Resolved Friction Factor via Chilton–Colburn Formulation

For internal flows it is often more accurate—and much more faithful to the local hydrodynamics—to obtain mass transfer from the same near-wall momentum solution that determines skin friction. With the skin-friction coefficient  $C_f = 2\tau_w/(\rho U_b^2)$  (and  $f_D = 4C_f$ ), the Chilton–Colburn analogy gives the local or section-mean mass-transfer  $j$ -factor,

$$j_{D,i} \equiv \frac{\text{Sh}_i}{\text{Re} \text{Sc}_i^{1/3}} \approx \frac{C_f}{2} = \frac{f_D}{8}, \quad \Rightarrow \quad \text{Sh}_i \approx \frac{C_f}{2} \text{Re} \text{Sc}_i^{1/3}. \quad (17)$$

Equation (17) is the operative link between turbulence modeling and interfacial chemistry in our framework: any improvement in the prediction of  $u_*$  (through re-laminarization damping, buoyancy production  $G_b$ , roughness, or wall treatments) propagates directly into  $k_{m,i}$  via (13). Numerically, we compute  $C_f$  from the RANS wall shear, evaluate  $\text{Sh}_i$  from (17), and assemble  $k_{m,i}$ . This route automatically accounts for stabilizing (opposing) and destabilizing (aiding) buoyancy through the resolved  $\tau_w$ -field and avoids ad hoc Richardson-number corrections to  $\text{Sh}_i$ .

#### 4.1.3. Local vs. bulk, transitional blending, and development.

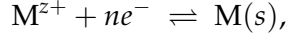
The film coefficient in (13) should be interpreted locally at each wall quadrature point. In *developing* flows,  $\text{Sh}_i$  should be based on a local entrance coordinate  $x$  or on a CFD-inferred development measure; in practice we blend a developing-flow estimate of the form  $\propto (\text{Re} \text{Sc}_i d_h/x)^{1/3}$  with the fully developed value using a smooth switch over a few hydraulic diameters. In *transitional* regimes ( $2000 \lesssim \text{Re} \lesssim 5000$ ) a logistic blend between laminar (15) and turbulent (16) values regularizes the coefficient; in the friction-factor route, the blending occurs implicitly through  $C_f$ . Roughness and re-laminarization effects are best handled by the friction route because  $C_f$  already reflects equivalent sand-grain roughness and low-Re damping in the turbulence model; using (16) with a roughness-corrected  $f_D$  is also acceptable when a correlation-based path is preferred.

#### 4.1.4. Coupling to the species equation and PNP consistency.

The film law (13) is enforced as a Robin boundary condition on the liquid species equation (7),  $-\mathbf{n} \cdot (D_{i,\text{eff}} \nabla c_i) = k_{m,i} (c_{i,b} - c_{i,w})$ , where  $D_{i,\text{eff}} = D_i + \mu_t/(\rho \text{Sc}_{t,i})$  maintains consistency with the resolved turbulent diffusion. Because the electromigration term in (7) does not contribute to the normal diffusive flux at an insulating wall, the film law closes the liquid-side transport. In regions where the electroneutral approximation is valid, the dominant impact of turbulence on interfacial transport is through  $k_{m,i}$ ; in thin space-charge layers where Poisson coupling is retained, (13) still applies as the integral closure across the concentration sublayer adjacent to the double layer. Finally, for multi-species problems with large  $\text{Sc}_i$  typical of molten salts, the  $\text{Sc}_i^{1/3}$  scaling in (17) implies that species with smaller diffusivity (larger  $\text{Sc}_i$ ) have proportionally smaller  $k_{m,i}$ , a fact that will be important when interpreting kinetic vs. mass-transfer control in Secs. 4.2.–4.3..

## 4.2. Butler–Volmer electro-kinetics and interpretation

We consider a single-charge-transfer half-reaction representative of metal dissolution/plating at a solid boundary,



with  $n = z$  for a simple cation reduction to the metal. Let  $\phi_s$  and  $\phi_\ell$  denote the electric potentials (V) in the solid and liquid, respectively. The *overpotential*

$$\eta \equiv (\phi_s - \phi_\ell) - E_{\text{eq}}(T, \mathbf{a}, \xi) \quad (18)$$

measures the departure from the reversible (Nernst) potential  $E_{\text{eq}}$  at the local temperature  $T$  and activities  $\mathbf{a} = \{a_i\}$  (with redox descriptor  $\xi$ ). For the reduction of  $\text{M}^{z+}$  to the pure solid  $\text{M}(s)$  (activity  $\approx 1$ ),

$$E_{\text{eq}}(T, \mathbf{a}, \xi) = E^\circ(T) + \frac{RT}{nF} \ln\left(\frac{a_{\text{M}^{z+}}}{a^\dagger}\right), \quad a_{\text{M}^{z+}} \equiv \gamma_{\text{M}^{z+}} \frac{c_{\text{M}^{z+}}}{c^\dagger}, \quad (19)$$

with  $F$  the Faraday constant,  $R$  the gas constant, and  $a^\dagger, c^\dagger$  reference activity/concentration (we take  $c^\dagger = 1 \text{ mol m}^{-3}$  so that  $a = \gamma c$  on a molar basis). In practice, our thermochemical solver (Thermochimica) returns the *equilibrium dissolved concentration*  $c_{\text{eq}}(T, \xi)$  consistent with (19); using  $c_{\text{eq}}$  avoids explicit evaluation of  $E_{\text{eq}}$  and guarantees thermodynamic consistency with the liquid composition.

### 4.2.1. Butler–Volmer rate law (kinetic control).

Under kinetic control (no liquid-side mass limitation), the interfacial current density ( $\text{A m}^{-2}$ ) is

$$i = i_0 \left[ \exp\left(\frac{\alpha_a n F \eta}{RT}\right) - \frac{a_{\text{M}^{z+}}}{a_{\text{M}^{z+}, \text{eq}}} \exp\left(-\frac{\alpha_c n F \eta}{RT}\right) \right], \quad (20)$$

where  $\alpha_a$  and  $\alpha_c$  are anodic and cathodic transfer coefficients ( $0 < \alpha_{a,c} < 1$ ), and  $i_0$  is the *exchange current density*. For the metal/ion couple it is convenient to write (20) on a *concentration* (molar) basis using  $a = \gamma c$  and  $a_{\text{M}^{z+}, \text{eq}} = \gamma_{\text{eq}} c_{\text{eq}}$ :

$$i = n F k_0 \left[ \gamma c e^{-\alpha_c n F \eta / (RT)} - \gamma_{\text{eq}} c_{\text{eq}} e^{+\alpha_a n F \eta / (RT)} \right], \quad i_0 = n F k_0 \gamma_{\text{eq}} c_{\text{eq}}, \quad (21)$$

with  $k_0$  an intrinsic (standard) surface rate coefficient ( $\text{m s}^{-1}$ ). Equation (21) makes transparent the unit consistency on a molar basis and the link

$i_0 = n F k_0 c_{\text{eq}}$  for  $\gamma \approx \gamma_{\text{eq}} \approx 1$

(22)

commonly used in molten salts when activity coefficients are treated as weak functions over the operating window. The associated *molar* interfacial flux (positive for plating  $\text{M}^{z+} \rightarrow \text{M}(s)$ ) is simply

$$J = \frac{i}{nF} = k_0 \left[ \gamma c e^{-\alpha_c n F \eta / (RT)} - \gamma_{\text{eq}} c_{\text{eq}} e^{+\alpha_a n F \eta / (RT)} \right] [\text{mol m}^{-2} \text{s}^{-1}]. \quad (23)$$

In our sign convention  $J > 0$  denotes *plating* (net flux from liquid to solid), while  $J < 0$  denotes *dissolution*. If one prefers the electrochemical sign convention (anodic current positive), use  $i_{\text{anodic}} = -nFJ$ .

### 4.2.2. Physical interpretation.

Equation (21) is the sum of a forward (anodic) and a backward (cathodic) process that share an activation barrier whose height is shifted by the overpotential. The transfer coefficients  $\alpha_a$  and  $\alpha_c$  partition that barrier; for a symmetric barrier  $\alpha_a \approx \alpha_c \approx 1/2$ . At *equilibrium* ( $\eta = 0$  and  $c = c_{\text{eq}}$ ) the two exponentials are equal and opposite, so  $i = 0$  even though each branch carries the finite *exchange current*  $i_0$ . Close to equilibrium ( $|\eta| \ll RT/(nF)$  and  $c \approx c_{\text{eq}}$ ), linearization gives

$$i \approx i_0 \frac{(\alpha_a + \alpha_c) nF}{RT} \eta, \quad R_p \equiv \left( \frac{\partial i}{\partial \eta} \right)_{\eta=0}^{-1} = \frac{RT}{(\alpha_a + \alpha_c) nF i_0}, \quad (24)$$

so the small-signal *polarization resistance*  $R_p$  is set by  $i_0$  and the symmetry factor  $(\alpha_a + \alpha_c)$ . Far from equilibrium, one *Tafel branch* dominates:

$$\eta \ll -\frac{RT}{nF}: i \approx -i_0 \exp\left(-\frac{\alpha_c nF \eta}{RT}\right) \quad (\text{cathodic, plating}), \quad b_c = \frac{2.303 RT}{\alpha_c nF}, \quad (25)$$

$$\eta \gg \frac{RT}{nF}: i \approx +i_0 \exp\left(\frac{\alpha_a nF \eta}{RT}\right) \quad (\text{anodic, dissolution}), \quad b_a = \frac{2.303 RT}{\alpha_a nF}, \quad (26)$$

with  $b_{a,c}$  the usual Tafel slopes (V dec<sup>-1</sup>). The temperature dependence enters both through the exponential factors and through  $i_0(T)$ ; an Arrhenius form  $k_0(T) = k_\infty \exp(-E_a/RT)$  implies  $i_0(T) \propto c_{\text{eq}}(T) \exp(-E_a/RT)$ , so hotter surfaces generally exhibit larger exchange currents, modulated by the thermochemical response of  $c_{\text{eq}}(T, \xi)$ .

### 4.2.3. Consistency with PNP and thermochemistry.

The activity factor in (20) ensures that the kinetic law is invariant to the choice of concentration units and is thermodynamically consistent with the Poisson–Nernst–Planck transport (§3.). Using Thermochemica to compute  $c_{\text{eq}}(T, \xi)$  (and, if desired,  $\gamma$ ) guarantees that the reversible state ( $\eta = 0, c = c_{\text{eq}}$ ) is the same state realized by the liquid composition. In the next subsection we will couple (23) to the liquid–side film law to eliminate the unknown interfacial concentration  $c$  and obtain the *operational* current–overpotential relation that accounts for both kinetics and mass transfer.

### 4.2.4. Dimensional and sign checks.

With  $k_0$  in m s<sup>-1</sup> and  $c$  in mol m<sup>-3</sup>, the bracket in (23) has units mol m<sup>-3</sup> and  $J$  has units mol m<sup>-2</sup> s<sup>-1</sup>; multiplying by  $nF$  yields  $i$  in A m<sup>-2</sup>. By our convention  $J > 0$  (hence  $i > 0$ ) corresponds to net *plating* (liquid → solid). If one adopts the opposite electrochemical sign (anodic current positive), simply reverse the sign of  $i$  when reporting polarization curves.

## 4.3. Two-film formulation and derivation of the interfacial current

We now couple liquid–side mass transport to interfacial electro–kinetics to obtain an *operational* current–overpotential relation that accounts for both film transport and Butler–Volmer (BV) kinetics. We proceed in four steps: (i) write the 1-D steady Nernst–Planck flux across the liquid film and reduce it with electroneutrality to a *film law with migration*; (ii) impose Faradaic stoichiometry to relate the species flux to the interfacial current; (iii) combine with the BV rate law to eliminate the unknown interfacial concentration; and (iv) analyze the resulting expression, including limiting currents and asymptotic regimes.

### 4.3.1. Liquid film transport with migration.

Consider a thin normal layer  $y \in [0, \delta]$  from the wall ( $y = 0$ ) into the bulk ( $y = \delta$ ), with steady, 1-D transport, no homogeneous sources, and negligible normal convection. For an ionic species  $i$  (charge  $z_i$ ), the Nernst–Planck flux is

$$N_i = -D_i \frac{dc_i}{dy} - \frac{z_i D_i}{RT} c_i \frac{d\phi_\ell}{dy}, \quad i = F \sum_k z_k N_k \quad (\text{total current density}). \quad (27)$$

Under the standard electroneutral approximation inside the film ( $\sum_k z_k c_k = 0$ ), the electric field adjusts so that the migration terms carry a fixed fraction of the total current. Introducing the *transference number*  $t_i$  (fraction of the current carried by species  $i$ , treated here as locally constant across the film),

$$\sum_k t_k = 1, \quad F z_i N_i^{(\text{mig})} = t_i i, \quad (28)$$

the steady flux  $N_i$  can be re-written in the *concentrated-solution* form

$$N_i = -D_i \frac{dc_i}{dy} + \frac{t_i}{z_i F} i, \quad (29)$$

which is equivalent to eliminating  $d\phi_\ell/dy$  between the set (27) using electroneutrality. In a thin film with piecewise-constant coefficients and a constant flux, integration of (29) across  $y \in [0, \delta]$  yields the *film law with migration*:

$$N_i = k_{m,i} (c_{i,b} - c_{i,w}) + \frac{t_i}{z_i F} i, \quad k_{m,i} \equiv \frac{D_i}{\delta} \quad \text{or} \quad k_{m,i} = \frac{\text{Sh}_i D_i}{d_h} \quad (\text{CFD/correlation}). \quad (30)$$

Here  $c_{i,w}$  is the liquid-side interfacial concentration,  $c_{i,b}$  a near-wall bulk value, and  $k_{m,i}$  is the film (liquid-side) mass-transfer coefficient obtained either from correlations or from the friction-factor route in Sec. 4.1.. Equation (30) reduces to the classical two-film law when  $t_i \rightarrow 0$  (strong supporting electrolyte) and recovers the well-known  $(1 - t_i)$  enhancement of the diffusion-limited current when electromigration is important.

### 4.3.2. Faradaic stoichiometry at the interface.

Consider the single-step metal reduction/plating half-reaction



with the sign convention that the *molar interfacial rate*  $J > 0$  corresponds to net *plating* (liquid  $\rightarrow$  solid). Faraday's law gives

$$i = n F J, \quad \text{and} \quad N_{\text{M}^{z+}} = J \quad (\text{consumption of the cation at the wall}). \quad (31)$$

Specializing (30) to the reacting cation  $i = \text{M}^{z+}$  with  $z_i = n$  and  $t_i \equiv t_+$ , and using (31), we obtain the key algebraic relation between the interfacial concentration  $c_w \equiv c_{\text{M}^{z+},w}$  and the current:

$$i (1 - t_+) = n F k_m (c_b - c_w), \quad \Rightarrow \quad c_w = c_b - \frac{(1 - t_+)}{n F k_m} i. \quad (32)$$

In the limit  $t_+ \rightarrow 0$  this reduces to the familiar  $i = n F k_m (c_b - c_w)$ . Equation (32) embodies the *film* and *migration* constraints and will be used to eliminate  $c_w$  from the BV kinetics.

### 4.3.3. Coupling to Butler–Volmer and elimination of $c_w$ .

The BV flux on a molar basis (Sec. 4.2.) for this couple is

$$J = k_0 \left[ \gamma_w c_w e^{-\alpha_c \tilde{\eta}} - \gamma_{\text{eq}} c_{\text{eq}} e^{+\alpha_a \tilde{\eta}} \right], \quad \tilde{\eta} \equiv \frac{nF\eta}{RT}, \quad (33)$$

with  $k_0$  the intrinsic surface rate ( $\text{m s}^{-1}$ ),  $\gamma_w$  the activity coefficient at the wall (often  $\approx \gamma_b$ ), and  $c_{\text{eq}}(T, \xi)$  the thermochemically consistent equilibrium concentration. Multiplying (33) by  $nF$  gives the kinetic current

$$i = nFk_0 \left[ \gamma_w c_w e^{-\alpha_c \tilde{\eta}} - \gamma_{\text{eq}} c_{\text{eq}} e^{+\alpha_a \tilde{\eta}} \right]. \quad (34)$$

Substituting (32) into (34) yields an equation *linear* in  $i$ :

$$\begin{aligned} i &= nFk_0 \left[ \gamma_w \left( c_b - \frac{(1-t_+)}{nFk_m} i \right) e^{-\alpha_c \tilde{\eta}} - \gamma_{\text{eq}} c_{\text{eq}} e^{+\alpha_a \tilde{\eta}} \right] \\ &= nFk_0 \left[ \gamma_w c_b e^{-\alpha_c \tilde{\eta}} - \gamma_{\text{eq}} c_{\text{eq}} e^{+\alpha_a \tilde{\eta}} \right] - \underbrace{\left( \frac{k_0 \gamma_w}{k_m} (1-t_+) e^{-\alpha_c \tilde{\eta}} \right) i}_{\Phi_c(\eta)}. \end{aligned} \quad (35)$$

Rearranging, we obtain the *closed* current–overpotential relation that accounts for (i) kinetics, (ii) mass transfer, and (iii) migration through  $t_+$ :

$$i(\eta) = \frac{nFk_0 \left[ \gamma_w c_b e^{-\alpha_c \tilde{\eta}} - \gamma_{\text{eq}} c_{\text{eq}} e^{+\alpha_a \tilde{\eta}} \right]}{1 + \frac{k_0 \gamma_w}{k_m} (1-t_+) e^{-\alpha_c \tilde{\eta}}}. \quad (36)$$

All symbols are known at the wall:  $k_m$  (from Sec. 4.1.),  $k_0, \alpha_{a,c}$  (kinetics),  $c_b$  (near-wall bulk),  $c_{\text{eq}}, \gamma$  (thermochemistry), and  $t_+$  (either specified, computed from PNP, or approximated).

### 4.3.4. Analysis: limiting currents and asymptotic regimes.

Equation (36) recovers the correct limits:

*Reaction-limited* ( $k_m \rightarrow \infty$  or  $\text{Da}_m \equiv k_0 \gamma_w / k_m \rightarrow 0$ ). The denominator  $\rightarrow 1$  and

$$i \rightarrow nFk_0 \left[ \gamma_w c_b e^{-\alpha_c \tilde{\eta}} - \gamma_{\text{eq}} c_{\text{eq}} e^{+\alpha_a \tilde{\eta}} \right] \equiv i_{\text{BV}}(\eta; c_b), \quad (37)$$

i.e., the classical Butler–Volmer law with the *bulk* concentration as the reactant activity (because  $c_w \rightarrow c_b$ ).

*Mass-transfer-limited cathodic branch* ( $\eta \rightarrow -\infty$ ). Then  $e^{-\alpha_c \tilde{\eta}} \rightarrow \infty$ ,  $e^{+\alpha_a \tilde{\eta}} \rightarrow 0$ ; the ratio in (36) tends to a finite limit:

$$i \rightarrow \boxed{i_{\lim,c} = \frac{nFk_m}{1-t_+} c_b} \quad (\text{diffusion/migration-limited current}). \quad (38)$$

This is precisely the Nernst diffusion–layer result with electromigration enhancement by  $(1-t_+)^{-1}$ . It corresponds to  $c_w \rightarrow 0$  in (32).

*Strong anodic branch* ( $\eta \rightarrow +\infty$ ). Then  $e^{-\alpha_c \tilde{\eta}} \rightarrow 0$  and the denominator  $\rightarrow 1$ . The current becomes

$$i \sim -nFk_0 \gamma_{\text{eq}} c_{\text{eq}} e^{+\alpha_a \tilde{\eta}} \quad (\text{with our sign convention, positive } i \text{ denotes plating}), \quad (39)$$

i.e., reaction-controlled dissolution. Mass transfer of the product cation enters *indirectly* by modifying the local thermodynamic state; if  $E_{\text{eq}}$  is evaluated with the wall composition (recommended), product accumulation reduces the effective overpotential for a given applied potential.

*Mixed control and Damköhler numbers.* Define a *mass-transfer Damköhler number* for the cathodic branch,

$$\text{Da}_m(\eta) \equiv \frac{k_0 \gamma_w}{k_m} (1 - t_+) e^{-\alpha_c \tilde{\eta}}, \quad \Rightarrow \quad i(\eta) = \frac{i_{\text{BV}}^{(c)}(\eta) - i_{\text{BV}}^{(a)}(\eta)}{1 + \text{Da}_m(\eta)}, \quad (40)$$

with  $i_{\text{BV}}^{(c)} = nFk_0 \gamma_w c_b e^{-\alpha_c \tilde{\eta}}$  and  $i_{\text{BV}}^{(a)} = nFk_0 \gamma_{\text{eq}} c_{\text{eq}} e^{+\alpha_a \tilde{\eta}}$ . When  $\text{Da}_m \ll 1$  the response is kinetic; when  $\text{Da}_m \gg 1$  the response saturates to  $i_{\text{lim},c}$ .

#### 4.3.5. Generalization to multi-species stoichiometry.

For a general half-reaction  $\sum_j \nu_j \text{Ox}_j + ne^- \rightleftharpoons \sum_r \nu_r \text{Red}_r$  (all  $\nu > 0$ ), with  $\nu_j$  moles of reactant  $j$  consumed per  $n$  electrons, the interfacial molar rate is  $J = i/(nF)$ . Each reacting ionic species  $q$  satisfies

$$N_q = \nu_q J = k_{m,q} (c_{q,b} - c_{q,w}) + \frac{t_q}{z_q F} i \quad \Rightarrow \quad c_{q,w} = c_{q,b} - \frac{\nu_q}{nF k_{m,q}} i + \frac{t_q}{z_q F k_{m,q}} i. \quad (41)$$

The BV law (in activity form) involves the product of reactant and product activities; after substituting (41) for every ionic reactant appearing in the cathodic exponential (and, if desired, the activities of ionic products in the anodic term), one obtains a rational expression analogous to (36), with a denominator that contains a *sum* over reacting species,

$$1 + \sum_{q \in \mathcal{R}_{\text{cat}}} \frac{k_0 \gamma_{q,w}}{k_{m,q}} \left( \nu_q - \frac{t_q}{z_q} n \right) e^{-\alpha_c \tilde{\eta}} \quad (\text{for small activity variations, linear in } i), \quad (42)$$

and a numerator that retains the BV form but with all wall concentrations replaced by their bulk values. The single-ion reduction presented above is thus the special case  $\nu_q = 1$ ,  $z_q = n$ ,  $\mathcal{R}_{\text{cat}} = \{\text{M}^{z+}\}$ .

#### 4.3.6. Remarks on consistency with PNP and numerical coupling.

In a full PNP simulation, the wall value  $t_+$  can be computed from the local ionic mobilities and concentrations; (32) then enforces the correct balance between diffusion and electromigration in the thin normal layer that is under-resolved by the mesh. The overpotential  $\eta$  in (36) should use the *wall* liquid potential  $\phi_{\ell,w}$  and the solid potential  $\phi_s$  to avoid double counting ohmic drops in the electrolyte; any externally specified potential difference referenced to the bulk can be converted to an interfacial  $\eta$  by subtracting the PNP-resolved ohmic and diffusion potentials between bulk and wall. Numerically, (36) is explicit in  $i$ ; given  $(k_m, k_0, \alpha_{a,c}, t_+, c_b, c_{\text{eq}}, \gamma)$  and  $\eta$ , the current follows by direct evaluation, and the corresponding wall concentration  $c_w$  is recovered from (32). This algebraic closure delivers a robust interface condition for the species equation (Robin form) and for charge conservation, while rigorously preserving the mass-transfer and kinetic limits.

## 4.4. Interpretation of the derived current and details on the numerical implementation

The operational current–overpotential relation obtained in §4.3.,

$$i(\eta) = \frac{nFk_0 \left[ \gamma_w c_b e^{-\alpha_c \tilde{\eta}} - \gamma_{\text{eq}} c_{\text{eq}} e^{+\alpha_a \tilde{\eta}} \right]}{1 + \frac{k_0 \gamma_w}{k_m} (1 - t_+) e^{-\alpha_c \tilde{\eta}}}, \quad \tilde{\eta} \equiv \frac{nF \eta}{RT}, \quad (43)$$

encapsulates, in closed form, the coupling between interfacial kinetics (through  $k_0, \alpha_{a,c}$ ), liquid-side transport (through  $k_m$ ), and electromigration within the film (through  $t_+$ ). The numerator is the Butler–Volmer (BV) response evaluated with bulk reactant activity (because  $c_w$  has been eliminated), while the denominator accounts for the depletion of the interfacial reactant by finite mass transfer and for the migration share of the current. As  $\eta \rightarrow 0$  and  $c_b \rightarrow c_{\text{eq}}$  the expression reduces to a linear polarization with an *effective* exchange current reduced by film resistance; as  $\eta \rightarrow -\infty$  it saturates to the diffusion/migration-limited current. These features imply that  $i(\eta)$  is well behaved and monotone on each Tafel branch, a property that underpins robust numerical coupling.

Near equilibrium, setting  $c_b = c_{\text{eq}}$  and linearizing in  $\eta$  yields  $i(\eta) \approx [(\alpha_a + \alpha_c) nF / (RT)] i_0^{\text{eff}} \eta$ , where  $i_0^{\text{eff}} = i_0 / (1 + \Lambda)$  with  $i_0 = nFk_0 \gamma_{\text{eq}} c_{\text{eq}}$  and  $\Lambda = (k_0 \gamma_w / k_m)(1 - t_+)$ . Thus the small-signal polarization resistance is  $R_p^{\text{eff}} = RT / [(\alpha_a + \alpha_c) nF i_0^{\text{eff}}]$ , larger than the kinetic  $R_p$  by the factor  $(1 + \Lambda)$ . On the strongly cathodic branch, dividing numerator and denominator of (43) by  $e^{-\alpha_c \tilde{\eta}}$  shows a smooth transition from the kinetic Tafel law to the mixed-control knee and finally to  $i_{\text{lim},c} = \frac{nFk_m}{1-t_+} c_b$  as  $\tilde{\eta} \rightarrow -\infty$ . On the anodic branch the denominator tends to unity and the classical BV law is recovered, so dissolution remains reaction-controlled unless the product activities in the anodic term are themselves constrained by transport (which can be included analogously if needed). These asymptotics guarantee both physical credibility and numerical boundedness: for finite  $k_m$  the cathodic current cannot exceed  $i_{\text{lim},c}$ , and  $c_w = c_b - \frac{(1-t_+)}{nFk_m} i$  remains nonnegative automatically when (43) is used to compute  $i$ .

For tightly coupled PNP–RANS simulations the overpotential must be defined at the true interface to avoid double-counting ohmic drops. We therefore take  $\eta = (\phi_s - \phi_{\ell,w}) - E_{\text{eq}}(T, \xi)$ , where  $\phi_{\ell,w}$  is the liquid potential evaluated at the wall quadrature point and  $E_{\text{eq}}$  (or, equivalently,  $c_{\text{eq}}$ ) is returned by the thermochemical model at the wall temperature and redox state. The bulk value  $c_b$  is the liquid concentration interpolated from the first off-wall control volume to the quadrature point in a manner consistent with the species discretization. The liquid-side mass-transfer coefficient is computed locally from either correlations (§4.1., fully developed or developing) or from the friction route via the resolved wall shear; because  $k_m \propto \text{Sh} D / d_h$  and  $\text{Sh} \sim (C_f/2) \text{Re} \text{Sc}^{1/3}$ , any turbulence-model correction to  $u_\star$  propagates directly into  $i(\eta)$  without additional closures.

There are two practical driving modes. In potentiostatic operation, the solid potential on the electrode boundary is prescribed (or the potential difference is imposed globally), and  $\eta$  is computed from the current liquid state; the interfacial current then follows from (43). In galvanostatic operation, an integral constraint enforces the net current, and a Lagrange multiplier adjusts  $\phi_s$  until  $\int_\Gamma i(\eta) dA = I_{\text{set}}$ ; the local  $i(\eta)$  still follows (43) pointwise. In either case the boundary fluxes are assembled consistently: the reacting ionic species receives a Neumann flux  $-\mathbf{n} \cdot \mathbf{J}_{M^{z+}} = J = i / (nF)$ , nonreacting ions have zero interfacial production (*unless* multi-species stoichiometry is modeled, in which case stoichiometric fluxes are applied), the solid satisfies  $-\mathbf{n} \cdot (\sigma_s \nabla \phi_s) = i$ , and the electrolyte current continuity is enforced by either prescribing the conduction current  $+\mathbf{n} \cdot \mathbf{i}_{\text{cond}} = i$  or, in a purely potentiostatic formulation, by leaving  $\phi_\ell$  free while enforcing the species fluxes (charge conservation then closes through PNP in the thin layer). Joule heating is included via

$q_J = \mathbf{i}_{\text{cond}} \cdot \mathbf{E}$  in the liquid and  $q_{J,s} = \sigma_s |\nabla \phi_s|^2$  in the solid; the convective current  $\rho_e \mathbf{u}$  does not dissipate and is excluded from  $q_J$ .

A monolithic Newton solve benefits from analytic sensitivities. Writing  $A \equiv nFk_0\gamma_w c_b$ ,  $B \equiv nFk_0\gamma_{\text{eq}}c_{\text{eq}}$ ,  $\Lambda \equiv (k_0\gamma_w/k_m)(1 - t_+)$ ,  $\theta \equiv \tilde{\eta} = nF\eta/(RT)$ , and  $D \equiv 1 + \Lambda e^{-\alpha_c \theta}$ , one has  $i = (Ae^{-\alpha_c \theta} - Be^{+\alpha_a \theta})/D$ . Differentiation gives

$$\frac{\partial i}{\partial \eta} = \frac{nF}{RT} \frac{[-\alpha_c Ae^{-\alpha_c \theta} - \alpha_a Be^{+\alpha_a \theta}]D - (Ae^{-\alpha_c \theta} - Be^{+\alpha_a \theta})(-\alpha_c \Lambda e^{-\alpha_c \theta})}{D^2}, \quad (44)$$

$$\frac{\partial i}{\partial c_b} = \frac{nFk_0\gamma_w e^{-\alpha_c \theta}}{D}, \quad \frac{\partial i}{\partial k_m} = \frac{\Lambda e^{-\alpha_c \theta}}{k_m} \frac{Ae^{-\alpha_c \theta} - Be^{+\alpha_a \theta}}{D^2} = \frac{\Lambda e^{-\alpha_c \theta}}{k_m} \frac{i}{D}, \quad (45)$$

$$\frac{\partial i}{\partial t_+} = \frac{\Lambda e^{-\alpha_c \theta}}{1 - t_+} \frac{i}{D}, \quad \frac{\partial i}{\partial \theta} = \frac{\partial i}{\partial \eta} \frac{RT}{nF}, \quad (46)$$

and, via chain rules,  $\partial i / \partial T$  follows from  $\partial \theta / \partial T = -(nF\eta)/(RT^2)$  together with the temperature dependences of  $k_0(T)$ ,  $c_{\text{eq}}(T, \xi)$ , and, if modeled,  $\gamma(T, \{c\})$ . The wall concentration recovered from  $c_w = c_b - \frac{(1-t_+)}{nFk_m} i$  inherits these sensitivities, for example  $\partial c_w / \partial \eta = -\frac{(1-t_+)}{nFk_m} \partial i / \partial \eta$  and  $\partial c_w / \partial c_b = 1 - \frac{(1-t_+)}{nFk_m} \partial i / \partial c_b$ . Incorporating (44)–(45) into the boundary residuals yields quadratic convergence without ad hoc under-relaxation in most regimes; when operating very near  $i_{\text{lim},c}$  a mild damping of the  $\eta$  update or a cap  $i \leftarrow \min(i, i_{\text{lim},c}(1 - \varepsilon))$  with  $\varepsilon \sim 10^{-6}$  prevents negative  $c_w$  under roundoff.

From a discretization standpoint the cleanest implementation treats (43) as the definition of the interfacial current at quadrature points, assembles the species Neumann flux for the reacting ion as  $J = i/(nF)$ , and uses the same  $i$  to impose the solid-current boundary condition. The liquid potential is best handled in a potentiostatic setting by directly forming  $\eta$  from  $(\phi_s - \phi_{\ell,w}) - E_{\text{eq}}$ ; in galvanostatic problems, a global current constraint determines  $\phi_s$  while the local  $i(\eta)$  enforces pointwise consistency with transport and kinetics. Care must be taken to use the *conduction* current in the Joule term and to evaluate  $k_m$  and  $c_b$  at the same quadrature locations and time levels as the species flux to avoid spurious source/sink imbalances. Finally, because  $k_m$  depends on  $C_f$  and thus on  $u_*$ , the turbulence model (including re-laminarization and buoyancy corrections) must be converged to a consistent wall shear before freezing  $k_m$  in a segregated update; in fully coupled solves,  $k_m$  should be recomputed from the current iterate at every nonlinear step so that improvements in near-wall momentum are immediately reflected in the electrochemical boundary condition.

In summary, the closed form (43) provides an algebraic, strictly bounded map from local thermodynamic state and near-wall hydrodynamics to interfacial current. Its linearization is explicit, its asymptotics recover the correct kinetic and mass-transfer limits, and its numerical realization aligns naturally with the weak forms of PNP, heat transfer, and RANS. This combination yields a robust and thermodynamically consistent interface model for molten-salt reactor chemistry.

## 5. DEMONSTRATION FOR THE LOTUS MOLTEN SALT REACTOR

This section demonstrates how the previously-developed interface current is applied in the context of multiphysics simulations of MRSs. For this purpose, an open source version of the Molten Chloride Reactor Experiment (MCRE), which uses a  $NaCl - UCl_3$  fuel salt and has been developed by the authors as a platform for model testing, is utilized. The next section summarize key aspects of the model developed, discuss the corrosion and plating aspects tested by this model, and presents the main results of the model.

### 5.1. Simulation setup for the open-source MCRE demonstration case

The complete neutronics and thermal-hydraulics open-source model of MCRE can be found in previous work from the authors [35]. Only a brief summary of the important thermal-hydraulics aspects of this model and the relevant conditions for species tracking are described in this section.

The flow and chemistry are solved on a three-dimensional mesh imported from `MCRE_mesh_fine.e` and uniformly scaled from millimeters to meters (factor  $10^{-3}$ ). The computational domain comprises four fluid subdomains—reactor, pipe, pump, and a thin `boundary_layer` region generated along all wetted surfaces—and one solid subdomain `reflector` (only in the primary app). The wall boundaries are collected as `wall-pipe`, `wall-pump`, `wall-reactor-caps`, and `wall-reactor-reflector`. A convenience sideset `reactor_bot` is defined on the reactor's bottom plane,  $x < 0$ , and is used to postprocess volumetric flow rate. A reactor bore of radius  $R = 0.2575$  m (area  $A = \pi R^2$ ) is used consistently when forming Reynolds and Nusselt/Sherwood groups via the hydraulic diameter  $d_h = 2R$ . The thermochemistry (`Thermochimica`) application replicates the fluid blocks (reactor, pipe, pump, `boundary_layer`) and deletes the solid `reflector` to focus on the liquid composition.

The liquid salt is modeled with incompressible RANS finite-volume Navier–Stokes (PIMPLE algorithm with Rhie–Chow stabilization), coupled to a two-equation  $k - \epsilon$  closure with re-laminarization enabled and buoyancy production  $G_b(T)$ . Energy is solved in both fluid ( $T$ ) and solid ( $T_s$ ) with conjugate heat transfer at `wall-reactor-reflector`. Six delayed-neutron-precursor (DNP) groups ( $c_1 \dots c_6$ ) are transported by advection–diffusion–decay with volumetric fission sources. Twelve scalar species are transported in the primary app: noble metals {Ru, Rh, Pa, Ag} in both liquid ( $\ell$ ) and solid ( $s$ ) fields, and structural-alloy constituents {Cr, Fe, Ni} likewise in liquid and solid. For all liquid species, molecular diffusion  $D_\ell$  is augmented by turbulent diffusion  $D_t = \mu_t / (\rho S_{ct})$  to form  $D_{\text{eff}} = D_\ell + D_t$ . Source terms for fission-product generation (Ru, Rh, Pa, Ag) are mapped from a neutronics `power_density` field. Interfacial mass transfer at `wall-reactor-reflector` is imposed with a mixed film–kinetics boundary condition (`LinearFVCoupledMassHeatTransferBC`) for each species pair (liquid  $\leftrightarrow$  solid), using local turbulence quantities to build the Sherwood number and a Butler–Volmer-like kinetic parameterization where appropriate. The `Thermochimica` app solves equilibrium chemistry for {Na, Cl, Cr, Fe, Ni, Kr, Mo, U} using the MSTDB chloride dataset; it receives  $T$  and  $p$  from the primary app and returns equilibrium dissolved concentrations  $c_{\text{eq}}$  for Cr, Fe, Ni that are then used in the interfacial corrosion laws.

The operating point corresponds to low-MW power with forced circulation and gravity aligned with the streamwise  $x$ -direction. The salt properties and turbulence scalings are held constant in each time step except where noted. Table 1 summarizes the principal inputs used to set the flow, heat transfer, turbulence, species transport, and interfacial models.

Table 1. Modeled operating conditions and key parameters used in the MCRC case.

Category	Symbol / setting	Value / comment
Geometry	Reactor radius $R$	0.2575 m (hydraulic diameter $d_h = 0.515$ m)
Gravity	$\mathbf{g}$	(−9.81, 0, 0) m s <sup>−2</sup> (aiding/opposing buoyancy along $x$ )
Fluid density	$\rho, \rho_0$	3279 kg m <sup>−3</sup> (Boussinesq $\rho(T) = \rho - \alpha T$ )
Thermal expansion	$\alpha$	$3.26 \times 10^{-4}$ K <sup>−1</sup>
Dynamic viscosity	$\mu$	$5.926 \times 10^{-3}$ Pas
Thermal conductivity (fluid)	$k$	0.38 W m <sup>−1</sup> K <sup>−1</sup>
Heat capacity (fluid)	$c_p$	640 J kg <sup>−1</sup> K <sup>−1</sup>
Turb. Prandtl / Schmidt	$\text{Pr}_t, \text{Sc}_t$	0.9, 0.9 (all species)
Turbulence model	$k-\varepsilon$	$C_\mu = 0.09, \sigma_k = 1.0, \sigma_\varepsilon = 1.3, C_1 = 1.44, C_2 = 1.92$
Wall treatment	$\text{neq}$	nonequilibrium wall function; re-laminarization enabled
Heat exchange (fluid↔solid)	$h$	3500 W m <sup>−2</sup> K <sup>−1</sup> at <b>wall-reactor-reflector</b>
Solid (reflector)	$\rho_s, c_{p,s}, \lambda_s$	3580 kg m <sup>−3</sup> , 880 J kg <sup>−1</sup> K <sup>−1</sup> , 30 W m <sup>−1</sup> K <sup>−1</sup>
External solid BC	$T_s$ on <b>wall-reflector</b>	Dirichlet $T_s = 873$ K (cold boundary)
Pump forcing	body force in pump	$1.2 \times 10^4$ N m <sup>−3</sup> in $y$ -momentum
Fission power (map)	$P$	25 kW (power_density from neutronics file)
Fission energy	$E_f$	$3.2 \times 10^{-11}$ J/fission (for source normalization)
Liquid diffusivity	$D_\ell$	$2.1 \times 10^{-6}$ m <sup>2</sup> s <sup>−1</sup> (all tracked ions)
Solid diffusivity	$D_s$	$1.7 \times 10^{-10}$ m <sup>2</sup> s <sup>−1</sup> (all plated species)
DNP diffusion	$\mu_{\text{dnp}}$	$1.66 \times 10^{-2}$ m <sup>2</sup> s <sup>−1</sup> (effective)
Noble-metal yields	Ru,Rh,Pa,Ag	0.11, 0.03, 0.05, 0.004 (mol per mol-fission)
Time integration	$t_{\max}, \Delta t$	$10^4$ s, variable [0.1, 100] s (piecewise linear)
Pressure reference	pin	$p = 0$ at point (0.5, 0, 0) (gauge)

In the liquid, we solve incompressible RANS with Boussinesq buoyancy in momentum, advection-diffusion for  $T$ , six DNP scalars with advection, diffusion, fission sources and radioactive decay, and advection-diffusion for each chemical species with  $D_{\text{eff}} = D_\ell + \mu_t / (\rho \text{Sc}_t)$ . Turbulence equations for  $k$  and  $\varepsilon$  include wall-function terms, buoyancy production, and low-Re damping (re-laminarization). In the solid reflector we solve transient heat conduction with conjugate coupling to the fluid at **wall-reactor-reflector** and a fixed cold Dirichlet boundary on **wall-reflector**. The thermochemistry app is advanced every time step but does not solve transport; it evaluates equilibrium at each CV using the current  $T$  and  $p$  and outputs equilibrium dissolved totals  $c_{\text{eq}}$  for Cr, Fe, Ni, as well as auxiliary element totals and the chlorine potential  $\mu : \text{Cl}$ . Initial liquid compositions in the thermochemistry app are  $c_{\text{Na}} = 1.4046 \times 10^4 \cdot \delta_{\text{Cl}}$  mol m<sup>−3</sup> with  $\delta_{\text{Cl}} = 0.01$ ,  $c_{\text{Cl}} = 3.5083 \times 10^4$ ,  $c_{\text{U}} = 7012$ , and trace  $c_{\text{Cr,Fe,Ni,Kr,Mo}} = 10^{-3}$  mol m<sup>−3</sup>.

All velocity components satisfy no-slip on **wall-pipe**, **wall-pump**, **wall-reactor-caps**, and **wall-reactor-reflector**. Turbulent viscosity  $\mu_t$  uses a nonequilibrium wall-function boundary condition on the same walls, consistent with the  $k-\varepsilon$  closure. Pressure is pinned at a single point to set the gauge level. In the liquid energy equation, the **wall-reactor-reflector** boundary is treated as a conjugate interface: the fluid side imposes a convective heat-transfer BC using the local fluid and solid temperatures with  $h = 3500$  W m<sup>−2</sup> K<sup>−1</sup>; the solid side applies the reciprocal condition with the same  $h$ . The external solid boundary **wall-reflector** is isothermal at 873 K. All remaining fluid boundaries not explicitly specified are homogeneous Neumann (zero normal diffusive flux) for energy and scalar species.

For species, the only active interfacial mass exchange is at **wall-reactor-reflector**, where each liquid/solid pair is coupled by a two-film, turbulence-aware mass-transfer law augmented with electro-kinetic

terms:

**Noble metals plating:**  $\{\text{Ru, Rh, Pd, Ag}\}_\ell \rightleftharpoons \{\text{Ru, Rh, Pd, Ag}\}_s$ ,  
 $k_m = \frac{\text{Sh} D_\ell}{d_h}$ ,  
Sh built from local Re,  $\text{Sc}_t$ , and  $k$ ,  
 $c_{\text{eq}} = 0$  (no dissolved equilibrium concentration),  
 $i_0 = 10^{10} \text{ A m}^{-2}$  (kinetics quasi-instantaneous, mass-transfer limited).

**Structural alloy constituents corrosion:**  $\{\text{Cr, Fe, Ni}\}_\ell \rightleftharpoons \{\text{Cr, Fe, Ni}\}_s$ ,  
 $k_m = \frac{\text{Sh} D_\ell}{d_h}$  as above,  
 $c_{\text{eq}} = c_{\text{eq}}(T, p, \xi)$  from Thermochimica,  
electro-kinetic parameters:  $i_0 = 1 \text{ A m}^{-2}$ ,  
 $E_{\text{rxn}} = \{2.7, 2.5, 2.9\} \text{ V}$  for  $\{\text{Cr, Fe, Ni}\}$ ,  
 $\phi_{bc} = 2.5 \text{ V}$ ,  $n = 2$ , and local  $T$  enter the Butler–Volmer factor.

Each species uses `LinearFVCoupledMassHeatTransferBC` twice to enforce symmetry of liquid→solid and solid→liquid transport, with  $\{k, \text{Re}, \text{Sc}, D_\ell, d_h\}$  supplied pointwise as follows:  $k$  from the local  $k$ -field (TKE),  $\text{Re}$  from the run-time function  $\text{Re} = \dot{V}/A \cdot d_h/\mu$  using the instantaneous volumetric flow rate across `reactor_bot`,  $\text{Sc} = \text{Sc}_t$ ,  $D_\ell = 2.1 \times 10^{-6} \text{ m}^2 \text{ s}^{-1}$ , and  $d_h = 1.0 \text{ m}$  in the BC's internal scaling (the Sherwood construction still reflects the physical reactor diameter via the  $\text{Re}$  and  $k$  inputs). On all other walls, species default to zero-flux (impermeable). Within the liquid volume, noble metals  $\{\text{Ru, Rh, Pa, Ag}\}_\ell$  receive volumetric fission-product sources proportional to the mapped `fission_source`, with yields  $\{0.11, 0.03, 0.05, 0.004\}$  mol per mol-fission. Solid-phase species  $\{\text{Ru, Rh, Pa, Ag, Cr, Fe, Ni}\}_s$  diffuse with  $D_s = 1.7 \times 10^{-10} \text{ m}^2 \text{ s}^{-1}$  and otherwise exchange mass only through the interface.

The primary app advances one PIMPLE step per time step with segregated linear solves for momentum, pressure, turbulence, energy, solid energy, and passive scalars (species + DNP), using `hypre/boomerAMG` preconditioning and case-specific under-relaxation. After each time step, the fields  $T$  and  $p$  are transferred to the Thermochimica app, which computes  $c_{\text{eq}}$  for Cr, Fe, Ni and returns them at the beginning of the next step; these equilibrium concentrations enter the corrosion interfacial laws as the local thermodynamic reference. Postprocessors provide the instantaneous Reynolds number (from  $\dot{V}$  and  $\mu$ ), average heat-transfer coefficients, wall temperatures, temperature extrema and averages, reactor velocity magnitude (used as a bulk velocity proxy in the BCs), and integrated power-density measures. This setup ensures that the hydrodynamics (including re-laminarization and buoyancy effects) determine the local mass-transfer coefficients that, together with thermochemical equilibria, set the interfacial fluxes for plating (noble metals) and dissolution (structural alloy ions).

## 5.2. Thermochemical phenomena demonstrated by the open-source MCRE case

The demonstration couples turbulent advection–diffusion of tracer elements to an equilibrium thermochemistry solver, so that the local electrochemical driving forces at the metal–salt interface emerge from the actual temperature and composition of the circulating molten chloride. The key outcome is that the sign and magnitude of the interfacial current are determined by two *thermochemical* objects that vary in space and time:

the equilibrium dissolved concentration  $c_{i,\text{eq}}(T, p, \xi)$  of each alloying element  $i \in \{\text{Cr, Fe, Ni}\}$  returned by Thermochimica, and the chlorine chemical potential  $\mu_{\text{Cl}}$  that parameterizes the redox state  $\xi$  of the salt. In this configuration, hydrodynamics select the mass-transfer conductance  $k_{m,i}$ , while thermochemistry selects the reversible state; the interfacial kinetics merely interpolate between them.

Thermochimica is advanced on the same mesh blocks as the liquid and receives the instantaneous temperature field  $T(\mathbf{x}, t)$  and absolute pressure  $p(\mathbf{x}, t) = p_{\text{gauge}} + 10^5 \text{ Pa}$ . The chemical system includes  $\{\text{Na, Cl, Cr, Fe, Ni, Kr, Mo, U}\}$  with the MSTDB chloride dataset and outputs phase-resolved species and element totals. For corrosion modeling, the simulation collects the equilibrium *dissolved* chromium, iron, and nickel as

$$c_{\text{Cr,eq}} = [\text{CrCl}_2] + [\text{CrCl}_3], \quad c_{\text{Fe,eq}} = [\text{FeCl}_2] + [\text{FeCl}_3], \quad c_{\text{Ni,eq}} = [\text{NiCl}_2],$$

each in  $[\text{mol m}^{-3}]$ . These are transferred back to the flow solver and used directly in the interfacial law. The solver also computes an average  $\mu_{\text{Cl}}$ , which acts as a redox descriptor: raising  $\mu_{\text{Cl}}$  makes the environment more *oxidizing*, stabilizing higher chloride valences and increasing  $c_{i,\text{eq}}$ ; lowering  $\mu_{\text{Cl}}$  makes it more *reducing*<sup>4</sup>. Because the equilibrium is recomputed at the wall temperature, buoyancy-induced thermal stratification feeds back into  $c_{i,\text{eq}}(T)$  and thereby into the corrosion tendency.

The interface model used throughout the report can be written, on a molar basis and for a single ionic reactant, as the *operational* current-overpotential relation

$$i(\eta) = \frac{nFk_{0,i} \left[ \gamma_{i,w} c_{i,b} e^{-\alpha_{c,i}\tilde{\eta}} - \gamma_{i,\text{eq}} c_{i,\text{eq}} e^{+\alpha_{a,i}\tilde{\eta}} \right]}{1 + \frac{k_{0,i}\gamma_{i,w}}{k_{m,i}} (1 - t_{+,i}) e^{-\alpha_{c,i}\tilde{\eta}}}, \quad \tilde{\eta} = \frac{nF\eta}{RT}, \quad (47)$$

with the liquid-side film coefficient  $k_{m,i} = \text{Sh}_i D_i / d_h$  built from the local turbulence solution, the near-wall bulk concentration  $c_{i,b}$  coming from the transported species field, and the thermochemical equilibrium  $c_{i,\text{eq}}(T, p, \xi)$  coming from Thermochimica. In this test, activities are treated as  $\gamma \approx 1$  and migration is effectively suppressed ( $t_{+,i} \rightarrow 0$ ), so that the thermochemical and hydrodynamic dependences enter *only* through  $c_{i,\text{eq}}(T, p, \xi)$ ,  $c_{i,b}$ , and  $k_{m,i}$ . The overpotential is formed at the interface as  $\eta = (\phi_s - \phi_{\ell,w}) - E_{\text{eq}}(T, \xi)$ ; operationally, the input parameters  $\phi$  and  $E_{\text{reaction}}$  define a nominal bias, while  $c_{i,\text{eq}}$  ensures that the reversible state of the electrolyte is consistent with the local temperature and redox.

This setup demonstrates three coupled thermochemical phenomena in a way that is directly visible in the interfacial current. First, *redox control* by the chlorine potential sets the direction of mass transfer. At fixed  $\eta$ , increasing  $\mu_{\text{Cl}}$  raises  $c_{i,\text{eq}}$  and pushes the bracket in the numerator of (47) toward the anodic term, thereby making dissolution more favorable. Conversely, under more reducing conditions,  $c_{i,\text{eq}}$  falls, the cathodic term dominates, and plating or passivation is favored if  $c_{i,b}$  does not vanish. Because chromium forms the most stable chlorides among the three alloying elements over the operating window,  $c_{\text{Cr,eq}}$  rises fastest with oxidizing shifts, which is why, for identical kinetic parameters, chromium shows the largest corrosion tendency in the test; nickel, having the least favorable chloride stability, shows the smallest.

Second, *thermal speciation* couples to redox through the temperature field. The equilibrium constants for the M/Cl complexes are strongly temperature dependent; hotter surfaces (for example, where buoyant plumes impinge) tend to increase  $c_{i,\text{eq}}(T)$  and thus increase the reversible dissolution tendency locally. In the same regions, the hydrodynamics also raise the mass-transfer coefficient  $k_{m,i}$  (through larger  $u_*$  and  $C_f$ ), which reduces the denominator of (47) and further increases  $|i|$ . The test therefore exhibits a physically consistent co-localization of high  $c_{i,\text{eq}}$ , large  $k_{m,i}$ , and elevated corrosion current in plume-facing patches.

---

<sup>4</sup>A small "driving chlorine imbalance" is introduced in the initial sodium loading to bias  $\mu_{\text{Cl}}$  and demonstrate the sensitivity of  $c_{i,\text{eq}}$  to the redox state.

Third, *selective alloy dissolution* emerges from the combination of thermochemical equilibria and kinetic parameters. With the demonstration inputs  $E_{\text{reaction}} = \{2.7, 2.5, 2.9\}$  V for  $\{\text{Cr}, \text{Fe}, \text{Ni}\}$  and a common bias  $\phi \approx 2.5$  V, the electrical driving is weakest for chromium and strongest for iron if one holds  $E_{\text{eq}}$  fixed. However, because Thermochimica returns  $c_{i,\text{eq}}$  that differ by orders of magnitude, the net sign and size of the current are set primarily by the thermochemical term  $\gamma_{i,\text{eq}} c_{i,\text{eq}}$  in (47). Where  $c_{i,b} \approx c_{i,\text{eq}}$  and  $\eta \approx 0$ , the two exponentials cancel and the exchange current is recovered; where  $c_{i,b} < c_{i,\text{eq}}$  at the same  $\eta$ , the anodic branch dominates and dissolution proceeds. The demonstration thus makes explicit that "electrochemical corrosion" in molten salts is *thermodynamically* controlled by the local chloride chemistry, not just by an imposed potential difference.

The noble-metal plate-out is configured to isolate the hydrodynamic limit. For  $\{\text{Ru}, \text{Rh}, \text{Pa}, \text{Ag}\}$  the interfacial model sets  $c_{\text{eq}} = 0$  and a very large  $i_0$  (effectively  $k_0 \rightarrow \infty$ ), so the current reduces to the diffusion-limited form  $i_{\text{lim,c}} = nF k_m c_b$ . Thermochemistry is not used to cap the dissolved concentration of these species in this test; instead, their volumetric production is tied to the fission source and their deposition rate is governed entirely by the near-wall mass transfer. This contrast with the corrosion case is intentional: it highlights that plate-out of sparingly soluble or insoluble fission products is a *transport* problem, whereas alloy dissolution is a *thermochemical* problem modulated by transport.

Two implementation details complete the picture. The coupling is explicit-in-time but *thermodynamically consistent*: the fluid sends  $T$  and  $p$  at  $t^n$  to Thermochimica, which computes  $c_{i,\text{eq}}(T^n, p^n, \xi^n)$ ; those values are used to evaluate  $i(\eta)$  at  $t^{n+1}$ , so that the reversible state used in (47) always corresponds to the actually realized salt conditions. Moreover, because the same near-wall turbulence that sets  $k_{m,i}$  also shapes the temperature field, the redox/thermal and transport effects are not separable in the flow: plume–blanket asymmetries simultaneously alter  $c_{i,\text{eq}}(T)$  and  $k_{m,i}$ . The test therefore demonstrates, in a single configuration, (i) redox-controlled selectivity among  $\{\text{Cr}, \text{Fe}, \text{Ni}\}$  dissolution via  $c_{i,\text{eq}}(T, p, \xi)$ , (ii) transport-controlled plate-out of noble metals via  $k_m$ , and (iii) their nonlinear interaction through the full current law (47), including its kinetic, thermodynamic, and hydrodynamic terms.

### 5.3. Description of results

A critical factor influencing thermochemical processes within the molten salt reactor is the temperature distribution observed in both the fuel salt and the surrounding vessel. As illustrated in Figure 1, the temperature profile within the reactor core exhibits a notable increase as the salt traverses through the core. This temperature gradient is primarily driven by the heat generated from fission reactions, which is subsequently transferred to the circulating salt.

The principal cooling mechanism at play is the conjugate heat transfer between the molten salt and the reactor vessel. This interaction results in a temperature differential, causing the regions of salt adjacent to the vessel walls to cool more rapidly. Specifically, a pronounced cold spot emerges near the internal wall of the vessel, particularly evident on the right side of Figure 1. This phenomenon can be attributed to the circulation profiles established within the reactor core, where the flow dynamics influence heat distribution.

As the heated salt flows towards the vessel walls, it transfers thermal energy, resulting in a localized cooling effect. The temperature profile in both the vessel and reflector is thus governed by the effective cooling from the reactor core to the outer walls of the reflector. This thermal interaction is essential for maintaining optimal operating conditions and impacts the solubility and transport dynamics of various species within the salt. Furthermore, the temperature gradient plays a crucial role in dictating the electrochemical reactions occurring at the salt-metal interface, as the equilibrium concentrations of corrosion and plating species are highly dependent on temperature.

Consequently, understanding these temperature dynamics is key for accurately modeling the thermochemical behavior of the reactor system and predicting the stability and performance of the materials involved.

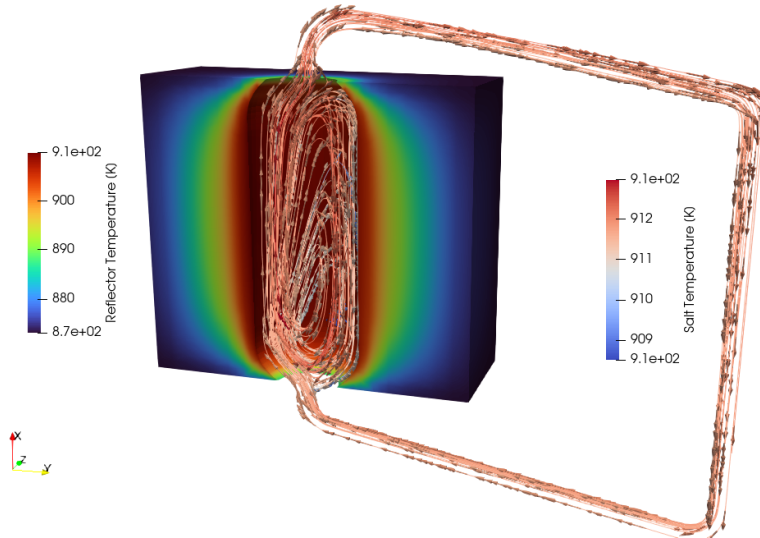


Figure 1. Flow streamlines colored with the fuel salt temperature field in the reactor core and the temperature field in the reactor vessel and reflector. The contours showcase the temperature profiles obtained within the reactor core, which govern the mass transport processes.

Another critical aspect in understanding the mass transfer coefficient within the reactor core is the complex flow phenomena that occur during operation. The characteristics of the flow dictate the friction factor adjacent to the walls, which also defines the mass exchange coefficient.

Figure 2 illustrates the evolution of streamlines concentrated around the inlet region of the reactor core. As depicted, the inlet flow profiles produce a jet that penetrates into the reactor core, resulting in the mixing and recirculation of the molten salt inside the reactor core. This jet is characterized by high momentum and velocity, which significantly influences the thermal and mass transfer processes within the system.

However, the flow instability associated with the expanding jet at the inlet to the reactor core lead to boundary layer tripping, resulting in an increased friction factor in the vicinity of the inlet. This phenomenon occurs due to the transition from a turbulent to a re-laminarized state as the jet interacts with the slower-moving fluid in the core. The tripping of the boundary layer enhances turbulence, which in turn substantially elevates the mass transfer coefficient in this region next to the inlet region. This enhanced mass transfer in the inlet will result on regions of considerable exchange next to this inlet region.

Moreover, the jet circulating towards the left side of the vessel, as shown in Figure 2, exhibits a different thermal behavior compared to the flow that descends along the right wall. The left-side jet does not have sufficient residence time against the wall to cool effectively, resulting in a higher temperature profile relative to the right wall. Consequently, this temperature differential leads to variations in chemical activity, with the left side exhibiting a higher chemical activity due to increased temperatures.

This disparity in temperature and chemical activity can significantly influence the electrochemical dynamics occurring at the liquid-solid interface, affecting processes such as corrosion and noble metal plating.

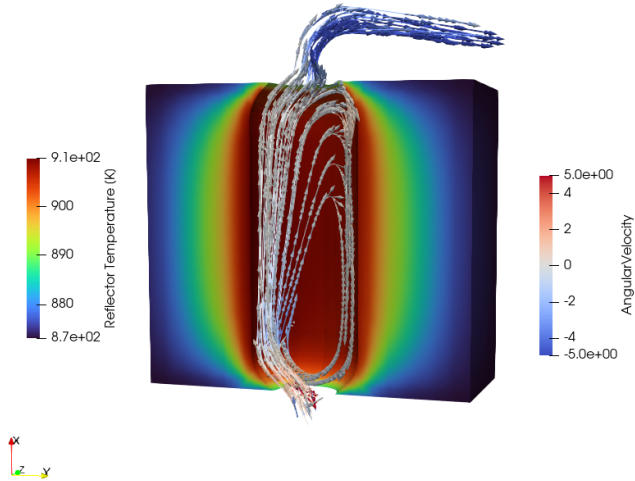


Figure 2. Flow streamlines around the inlet recirculation zone colored with the angular velocity and the temperature field in the reactor vessel and reflector. The figure showcases the detachment of the boundary layer at the reactor inlet, which results on a large friction factor before the tripping point and significant mass transfer in that region.

Although the flow and thermal fields within the reactor core reach a quasi-steady state in approximately 1,000 seconds, simulations are conducted over a longer time frame to assess the corrosion profiles developed in the reactor. Specifically, we model a total operational duration of 10 million seconds, or approximately 115.7 days.

The results for the three primary corrosion species—chromium, iron, and nickel—are presented in Figure 3. As expected, the concentration profiles for these species exhibit similar trends. However, as also expected, the contraction of chromium in the salt is higher than the iron one, which, in turn, is higher than the nickel one. This follows the behavior expected from the galvanic reduction potentials of each of these elements.

In all cases, the concentrations are relatively uniform throughout the bulk of the fuel salt, with slight increases near the vessel walls. This localized increase is attributed to the leaching of species from the vessel into the fuel salt, which has yet to diffuse through the boundary layer and fully mix within the reactor core.

Within the reactor vessel, a linear corrosion profile emerges, characterized by a higher defect of corrosion species adjacent to the fuel salt. Notably, an increased concentration of these species is observed near the tripping point of the boundary layer, where, as previously noted, enhanced mass transfer occurs alongside relatively elevated temperatures.

Furthermore, a more pronounced corrosion rate is computed on the left side of the domain compared to the right side in Figure 3. This disparity is primarily due to the higher chemical activity present in the hotter region on the left, which results in increased dissolution rates of the alloy constituents. In contrast, the cooler conditions on the right side lead to lower chemical activity and, consequently, reduced corrosion rates. No plating of corrosion products is observed on the cooler walls during the transient.

These findings underscore the importance of thermal and flow dynamics in influencing corrosion processes within the reactor, highlighting the need for careful consideration of these factors in future reactor designs and operational strategies.

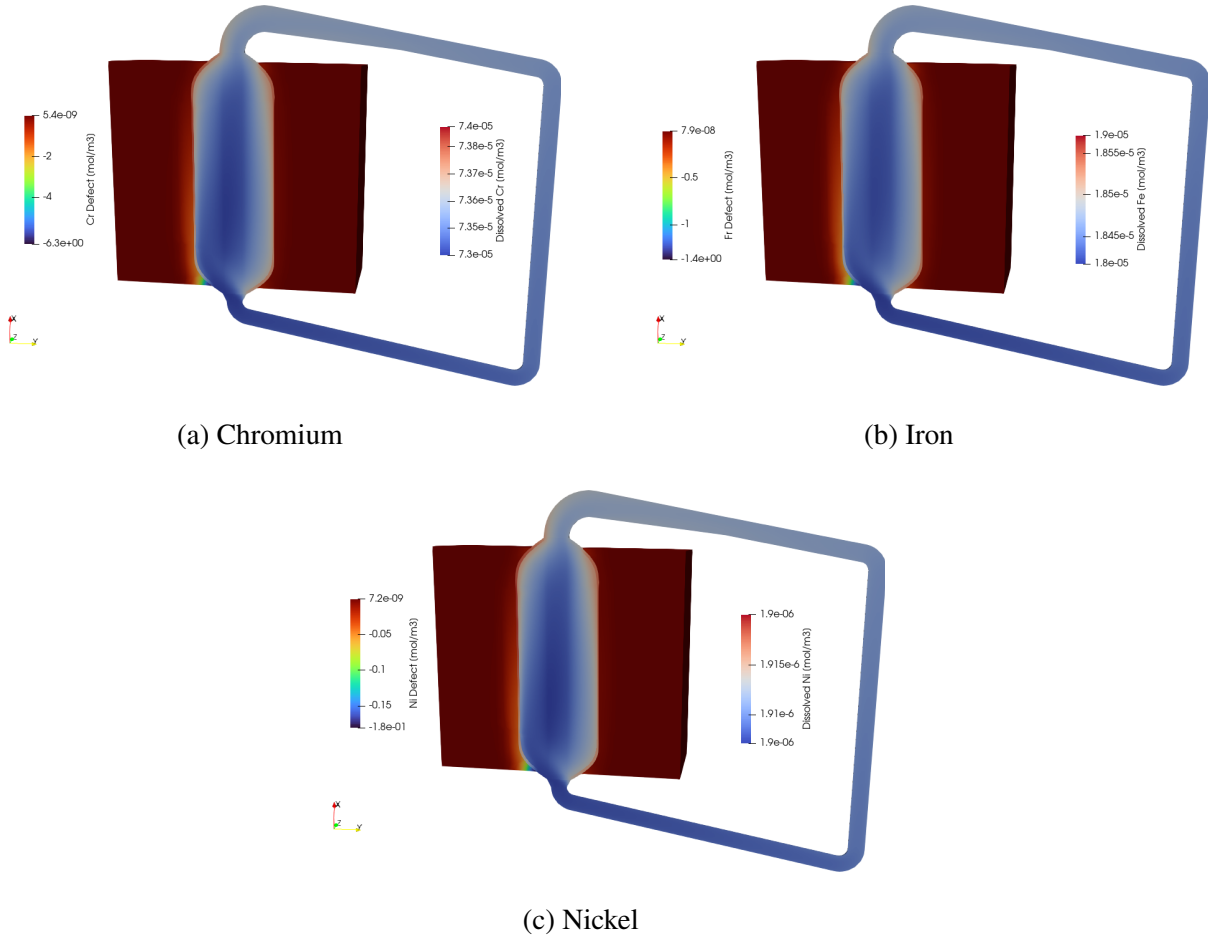


Figure 3. Distribution of corrosion species in the reactor core and reactor vessel between the reactor and the neutron reflector after 10,000,000 seconds ( $\sim 115.7$  days) of operation.

The results for noble metal plating at the end of the transient simulation are presented in Figure 4. Similar to the behavior observed for corrosion products, a comparable distribution pattern emerges for all noble metals. These noble metals are produced as fission products within the reactor core, subsequently migrating and depositing onto the reactor walls. Therefore, the magnitude of the distributions for each noble metal primarily depends on their respective fission yields.

The concentration of noble metals is generally uniform throughout the bulk of the fuel salt, with small reductions in concentration occurring near the vessel walls. This decrease is attributed to the plating of noble metals onto the reactor walls, which effectively removes them from the bulk salt solution. In this model, the extent of noble metal plating is significantly influenced by the mass exchange coefficient.

Upon examination of the plated noble metals within the vessel, a pronounced spike in concentration is observed near the tripping point of the boundary layer. This region is characterized by elevated friction factors and mass transfer coefficients, enhancing the deposition of noble metals. Furthermore, a large plating profile is noted along the left wall, which can be attributed to the increased friction factor resulting from the developing hydraulic jet conditions in that area. In contrast, a reduced plating intensity is observed along the right wall, where the lower friction factor is a consequence of the flow field being dominated by the comeback recirculation profile that returns from the core.

These findings highlight the crucial role of flow dynamics and mass transfer mechanisms in regulating

the deposition of noble metals in molten salt reactors, emphasizing the need for precise control of hydraulic conditions to optimize operational performance.

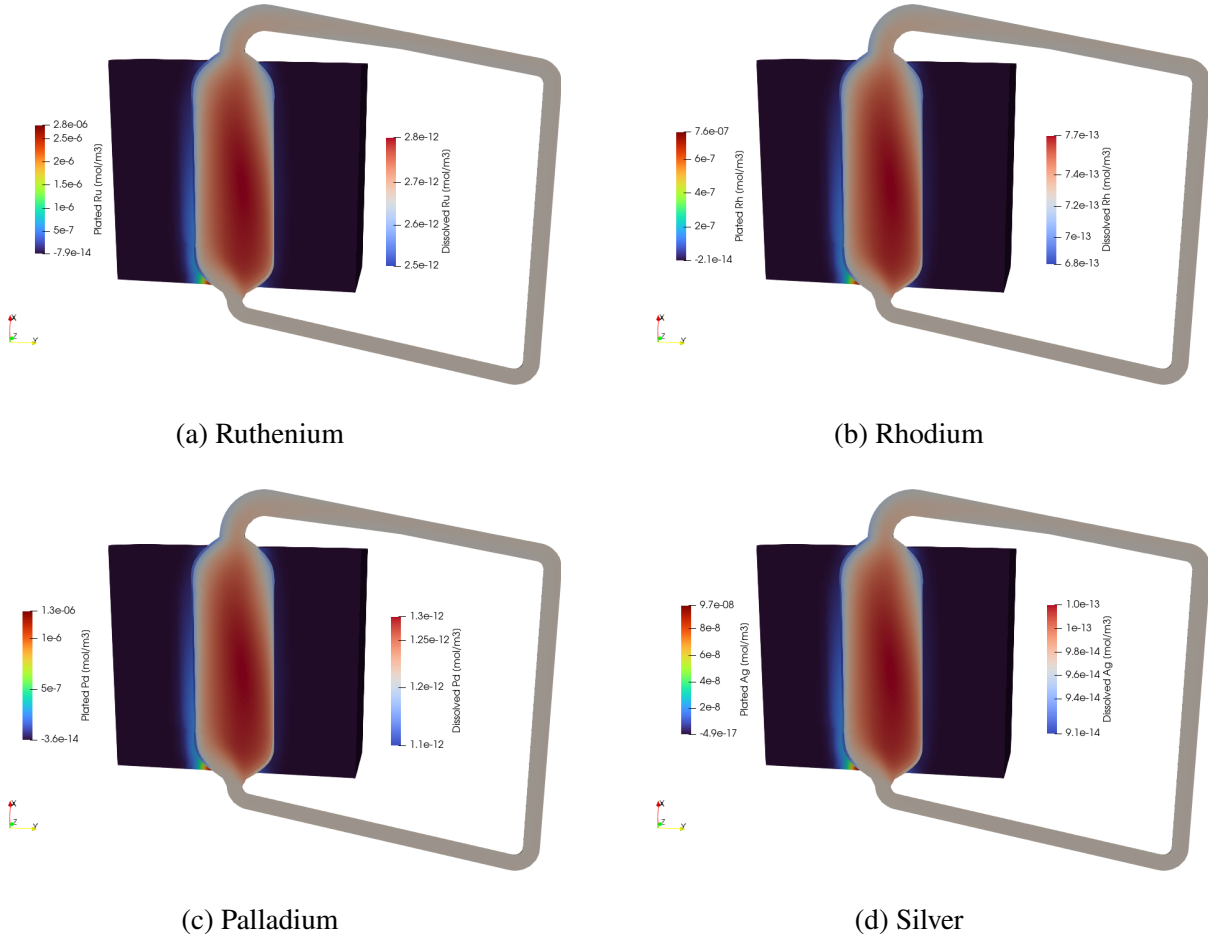


Figure 4. Distribution of plating species in the reactor core and reactor vessel between the reactor and the neutron reflector after 10,000,000 seconds ( $\sim 115.7$  days) of operation.

Finally, it is important to assess the evolution of corrosion and fission products throughout the transient operation of the reactor. For this analysis, chromium and ruthenium are selected as representative examples of a corrosion product and a noble metal plating species, respectively.

The temporal evolution of chromium concentration is illustrated in Figure 5. Initially, the concentration of chromium in the fuel salt experiences a rapid increase, driven by an excess of free chlorine present in the reactor core. However, as corrosion products accumulate, they consume the chemically available chlorine, leading to a significant reduction in corrosion rates over time. This behavior aligns with the corrosion kinetics typically observed for steel in molten salts, where the initial phase is characterized by an exponential growth in corrosion rates, followed by a slower, more linear increase as the reaction dynamics evolve.

In contrast, the plating profile of noble metals, exemplified by ruthenium in Figure 6, exhibits a more linear progression. Noble metals are continuously generated as fission products and subsequently transported to the reactor walls, where they undergo plating. Notably, the observed plating rate is substantially faster than the fission production rate, particularly at the relatively low power levels at which the open-source model of the MCRe operates. Consequently, the buildup rate of noble metals, such as ruthenium, reflects a nearly

linear trend over time.

These observations underscore the differing dynamics between corrosion and noble metal plating processes, highlighting the complex interplay between chemical species, thermal conditions, and hydrodynamic factors in determining the overall behavior of materials within molten salt reactors.

Figure 5. Evolution of Cr during operation transient. The evolution showcases a fast initial buildup with a corrosion rate stopping at later stages as free Chlorine is reduced by the corrosion products. *Note:* to display the animation Adobe Acrobat Reader or a similar viewing tool with animation capabilities is required.

Figure 6. Evolution of Ru during operation transient. The evolution showcases a liquid distribution reaching equilibrium, while the platted ruthenium builds up in the reactor vessel around the code. *Note:* to display the animation Adobe Acrobat Reader or a similar viewing tool with animation capabilities is required.

## 6. CONCLUSIONS AND FUTURE WORK

This report has explored the dynamics of corrosion and noble metal plating in MSRs, utilizing a MOOSE-based multiphysics modeling approach that integrates thermal-hydraulics-based transport phenomena, thermochemistry, and electrochemical kinetics. The findings from this study underscore the critical need for a detailed understanding of these processes to ensure the safe and efficient operation of MSRs.

In terms of **corrosion dynamics** our analysis of corrosion processes revealed that the behavior of structural alloys, particularly nickel-chromium-molybdenum alloys, is heavily influenced by the redox state and temperature of the molten salt. The results demonstrated a clear correlation between the availability of free chlorine and corrosion rates, with initial rapid increases in corrosion rates transitioning to slower, more linear increases as the chemically available chlorine was depleted. This behavior aligns with established corrosion kinetics observed in prior studies, highlighting the importance of managing chemical composition within the reactor to mitigate corrosion.

Regarding noble metal behavior the study of noble metal plating illustrated that these metals, generated as fission products, tend to migrate and deposit on reactor surfaces, significantly impacting material integrity. The distribution of noble metals in the molten salt was found to be relatively uniform, with localized concentration increases near the reactor walls due to plating. Notably, the mass exchange coefficient was identified as a key factor regulating noble metal deposition, with enhanced mass transfer occurring at regions of high fluid velocity and turbulence, particularly near the tripping point of the boundary layer.

Considering the **temperature and flow effects** on corrosion and plating rates, the coupling of temperature fields and flow dynamics was shown to play a vital role in both corrosion and noble metal behavior. The temperature gradients established within the reactor core influenced the solubility and transport dynamics of various species, while the flow profiles determined the friction factors and mass transfer coefficients essential for accurate modeling of these processes. The findings emphasized the need for precise control of hydraulic conditions to optimize both thermal performance and material interactions.

The implementation of the PNP framework, augmented with an interface current that integrates both mass- and electrochemically-driven transfer mechanisms, provided a comprehensive model for simulating the coupled processes occurring at the liquid-solid interface. This approach effectively captured the coupled evolution of species transport, electrochemical kinetics, and mass transfer, allowing for a more accurate representation of the interactions between the molten salt and structural materials. The utility of the MOOSE framework in developing tightly coupled multiphysics models was demonstrated, showcasing its capability to integrate various physical phenomena in a coherent manner.

The insights gained from this study have significant implications for the design and operation of future MSR systems. Understanding the mechanisms governing corrosion and noble metal plating will aid in developing strategies to enhance material performance, extend reactor lifetimes, and optimize operational parameters. The results also highlight the importance of continuous monitoring and management of chemical and thermal conditions within the reactor to mitigate corrosion risks and ensure the effective removal of noble metals.

In conclusion, this report contributes to the growing body of knowledge surrounding the behavior of materials in molten salt environments. By considering the coupled physics in the evolution of corrosion products and noble metal plating dynamics, we provide a foundation for future research and development efforts aimed at advancing the safety and efficiency of molten salt reactor technology.

The following areas of future work are recommended to further advance the understanding and optimization of corrosion and noble metal plating processes in molten salt reactors:

1. **Coupled Multi-Scale Simulations:** Develop multi-scale simulations that link microscopic (atomic-level) and mesoscale (phase-field) interactions with macroscopic reactor behavior. In particular, coupling mesoscale modeling can inform the effective diffusivity in the solid structures and the interface with the molten salt and provide a better-resolved interface mass current thanks to a higher resolution of the physics in the interface region. Additionally, this coupling can provide insights into how localized phenomena affect overall reactor performance and material integrity. This activity will be explored next fiscal year.
2. **Experimental Validation:** Conduct targeted experimental studies to validate the modeling predictions related to corrosion rates and noble metal plating behaviors. This includes long-term exposure tests under varying operational conditions to assess material performance and degradation mechanisms. An activity exploring the possibility of utilizing MSRE data as the initial validation base is planned for next fiscal year.
3. **Impact of Flow Dynamics:** Further study the impact of complex flow dynamics, such as turbulent mixing and stratification, on the transport of corrosion products and noble metals. This includes exploring how different flow configurations affect mass transfer coefficients and plating rates. In particular, this would involve informing the turbulence and mass transfer correlations used in Pronghorn with a higher fidelity tool like MOSCATO.
4. **Expanded Species Analysis:** Extend the modeling framework to include additional fission products and corrosion species of key interest, such as tellurium and iodine, to fully capture the nonlinear coupled dynamics in the molten salt environment and their effects on material interactions.
5. **Real-Time Monitoring Techniques:** Investigate the implementation of real-time monitoring techniques for corrosion and noble metal deposition within reactors. Techniques such as in-situ sensors could provide valuable data for adaptive control strategies to mitigate corrosion and optimize performance.
6. **Long-Term Operational Studies:** Perform long-duration operational simulations that simulate the cumulative effects of corrosion and noble metal plating over extended reactor lifetimes. This would provide insights into the long-term sustainability and reliability of MSR technologies.
7. **Optimization of Material Selection:** Investigate alternative materials and coatings that could enhance resistance to corrosion and noble metal deposition, focusing on the development of advanced alloys or composite materials tailored for molten salt environments.
8. **Integration with Reactor Design:** Collaborate with reactor design teams to incorporate findings from this study into the design and operational strategies of next-generation MSRs, ensuring that material considerations are integrated into the broader engineering framework.

## 7. REFERENCES

- [1] M. T. Retamales, S. Walker, and A. Abou-Jaoude, “Flow-informed corrosion in molten salts using the poisson-nernst-planck model,” in *20th International Topical Meeting on Nuclear Reactor Thermal Hydraulics, NURETH 2023*, pp. 3194–3207, American Nuclear Society, 2023.
- [2] P. N. Haubenreich and J. R. Engel, “Experience with the molten-salt reactor experiment,” *Nuclear Applications and Technology*, vol. 8, no. 2, pp. 118–136, 1970.
- [3] S. Guo, J. Zhang, W. Wu, and W. Zhou, “Corrosion in the molten fluoride and chloride salts and materials development for nuclear applications,” *Progress in Materials Science*, vol. 97, pp. 448–487, 2018.
- [4] D. F. Williams, L. M. Toth, and K. T. Clarno, “Assessment of candidate molten salt coolants for the advanced high-temperature reactor (ahtr),” Tech. Rep. ORNL/TM-2006/12, Oak Ridge National Laboratory, 2006.
- [5] D. E. Holcomb *et al.*, “An overview of liquid fluoride salt heat transport systems,” Tech. Rep. ORNL/TM-2010/156, Oak Ridge National Laboratory, 2010.
- [6] R. J. Kedl, “The migration of a class of fission products (noble metals) in the molten-salt reactor experiment,” Tech. Rep. ORNL-TM-3884, Oak Ridge National Laboratory, 1972.
- [7] E. L. Compere, E. G. Bohlmann, S. S. Kirslis, F. F. Blankenship, and W. R. Grimes, “Fission product behavior in the molten salt reactor experiment,” Tech. Rep. ORNL-4865, Oak Ridge National Laboratory, 1975.
- [8] J. R. Keiser, D. L. Manning, and R. E. Clausing, “Status of tellurium–hastelloy n studies in molten fluoride salts,” Tech. Rep. ORNL/TM-6002, Oak Ridge National Laboratory, 1977.
- [9] J. Busby *et al.*, “Technical assessment of materials compatibility in molten salt reactors,” Tech. Rep. ML21084A039, U.S. Nuclear Regulatory Commission, 2019.
- [10] S. A. Walker and W. Ji, “Species transport analysis of noble metal fission product transport, deposition, and extraction in the molten salt reactor experiment,” *Annals of Nuclear Energy*, vol. 158, p. 108250, 2021.
- [11] OECD/NEA, “Treatment of volatile fission products,” Tech. Rep. NEA/NSC/R(2022)4, Nuclear Energy Agency, 2022.
- [12] Z. Cheng, Y. Yang, G. Li, *et al.*, “The distribution and behavior of noble metal fission products ( $^{99}\text{mo}$ ,  $^{103}\text{ru}$ ,  $^{105}\text{rh}$ ,  $^{132}\text{te}$ ) in molten  $\text{LiF}-\text{BeF}_2$  mixtures,” *Journal of Nuclear Materials*, vol. 563, p. 153643, 2022.
- [13] S. Walker *et al.*, “Noble metal mass transport model for molten salt reactor experiment,” Tech. Rep. OSTI 1651415, U.S. Department of Energy / OSTI, 2019.
- [14] J. McFarlane *et al.*, “Fission product volatility and off-gas systems for molten salt reactors,” Tech. Rep. ORNL/SR-2019/129748, Oak Ridge National Laboratory, 2019.
- [15] J. McFarlane *et al.*, “Molten salt reactor engineering study for off-gas management,” Tech. Rep. ORNL/TM-2020/1640, Oak Ridge National Laboratory, 2020.

- [16] J. H. DeVan and R. B. E. III, “Corrosion behavior of reactor materials in fluoride salt mixtures,” Tech. Rep. ORNL-TM-328, Oak Ridge National Laboratory, 1962.
- [17] J. W. Koger, “Corrosion by fluoroborate salt: Mechanisms and analogies,” Tech. Rep. ORNL-TM-2978, Oak Ridge National Laboratory, 1970.
- [18] W. R. Grimes, “Chemical research and development for molten-salt breeder reactors,” Tech. Rep. ORNL-TM-1853, Oak Ridge National Laboratory, 1967.
- [19] M. Hong, H. L. Chan, J. R. Scully, and P. Hosemann, “Corrosion property of alloy 625 in molten flinak salt as a function of tellurium concentration,” *Journal of Nuclear Materials*, vol. 584, p. 154548, 2023.
- [20] S. S. Raiman and S. Lee, “Aggregation and data analysis of corrosion studies in molten chloride and fluoride salts,” *Journal of Nuclear Materials*, vol. 511, pp. 523–535, 2018.
- [21] R. N. Wright *et al.*, “Status of metallic structural materials for molten salt reactors,” Tech. Rep. INL/EXT-18-45171, Idaho National Laboratory, 2018.
- [22] O. Beneš and R. J. M. Konings, “Molten salt reactor fuel and coolant,” in *Comprehensive Nuclear Materials* (R. J. M. Konings, ed.), pp. 359–389, Elsevier, 2012.
- [23] R. R. Romatoski, “Fluoride salt coolant properties for nuclear reactor applications,” tech. rep., Massachusetts Institute of Technology, 2017.
- [24] J. Newman and K. E. Thomas-Alyea, *Electrochemical Systems*. Wiley, 3 ed., 2004.
- [25] A. J. Bard and L. R. Faulkner, *Electrochemical Methods: Fundamentals and Applications*. Wiley, 2 ed., 2001.
- [26] F. F. Blankenship, G. D. O’Kula, and R. E. Thoma, “A study of fission products in the molten-salt reactor experiment by gamma spectrometry,” Tech. Rep. ORNL-TM-3151, Oak Ridge National Laboratory, 1971.
- [27] M. Cho and colleagues, “Simulation model of molten salt corrosion using comsol.” Korean Nuclear Society Autumn Mtg. Preprint 23A-266, 2023.
- [28] H. L. Chan *et al.*, “Morphological evolution and dealloying during corrosion of ni–20cr in molten flinak,” *Journal of Nuclear Materials*, 2024. Early access.
- [29] H. B. Andrews *et al.*, “Review of molten salt reactor off-gas management,” Tech. Rep. OSTI 1831663, U.S. Department of Energy / OSTI, 2021.
- [30] T. Murakami *et al.*, “Electrorefining of metallic fuel with burnup ~7 at% in licl–kcl: Fission product behavior,” in *Journal of Nuclear Science and Technology (conference paper)*, 2018.
- [31] OECD/NEA, “Pyrochemical separations,” tech. rep., Nuclear Energy Agency, 2019.
- [32] M. S. Sohal *et al.*, “Conceptual design of forced convection molten salt heat transfer loop,” Tech. Rep. INL/EXT-10-18297, Idaho National Laboratory, 2010.
- [33] M. Tano, S. A. Walker, and A. Abou-Jaoude, “Flow-informed corrosion in molten salts using the poisson–nernst–planck model,” in *Proc. 20th Int. Topical Mtg. on Nuclear Reactor Thermal Hydraulics (NURETH-20)*, (Washington, D.C.), pp. 3194–3207, 2023.

- [34] A. M. Wheeler, O. Chvála, and S. Skutnik, “Initial calculations for source term of molten salt reactors,” *Annals of Nuclear Energy*, vol. 160, p. 108393, 2021.
- [35] M. Tano, R. Freile, R. de Oliveira, S. Walker, and A. Abou-Jaoude, “Coupled steady-state precursor distribution, and transients studies for open-core flow mcfrs,” Tech. Rep. INL/RPT-23-73982, Idaho National Laboratory, 2023.